The ALMaQUEST Survey XIV: do radial molecular gas flows affect the star-forming ability of barred galaxies?

L. M. Hogarth [1],[1]★ A. Saintonge [1],[1]★ T. A. Davis [1],[2] S. L. Ellison [1],[3] L. Lin,[4] C. López-Cobá,[4] H.-A. Pan[5] and M. D. Thorp[6]

[1]*University College London, Department of Physics & Astronomy, Gower Street, London WC1E 6BT, UK*
[2]*Cardiff Hub for Astrophysics Research & Technology, School of Physics & Astronomy, Cardiff University, Queens Buildings, Cardiff CF24 3AA, UK*
[3]*Dept. of Physics & Astronomy, The University of Victoria, Victoria, BC V8P 5C2, Canada*
[4]*Institute of Astronomy & Astrophysics, Academia Sinica, No. 1, Section 4, Roosevelt Road, Taipei 10617, Taiwan*
[5]*Department of Physics, Tamkang University, No.151, Yingzhuan Road, Tamsui District, New Taipei City 251301, Taiwan*
[6]*Argelander-Institut für Astronomie, Universität Bonn, Auf dem Hügel 71, 53121 Bonn, Germany*

ABSTRACT

We investigate whether barred galaxies are statistically more likely to harbour radial molecular gas flows and what effect those flows have on their global properties. Using 46 galaxies from the ALMA-MaNGA QUEnching and STar formation (ALMaQUEST) survey, we identify galaxies hosting optical bars using a combination of the morphological classifications in Galaxy Zoo 2 and HyperLEDA. In order to detect radial molecular gas flows, we employ full 3D kinematic modelling of the ALMaQUEST ^{12}CO(1–0) data cubes. By combining our bar classifications with our radial bar-driven flow detections, we find that galaxies classed as barred are statistically more likely to host large-scale radial gas motions compared to their un-barred and edge-on galaxy counterparts. Moreover, the majority of barred galaxies require multicomponent surface brightness profiles in their best-fitting models, indicative of the presence of resonance systems. We find that galaxies classed as barred with radial bar-driven flows ('barred + radial flow' subset) have significantly suppressed global star-formation efficiencies compared to barred galaxies without radial bar-driven flows and galaxies in the other morphological sub-samples. Our 'barred + radial flow' subset galaxies also possess consistently centrally concentrated molecular gas distributions, with no indication of depleted gas mass fractions, suggesting that gas exhaustion is not the cause of their suppressed star formation. Furthermore, these objects have higher median gas mass surface densities in their central 1 kpc, implying that central gas enhancements do not fuel central starbursts in these objects. We propose that dynamical effects, such as shear caused by large-scale inflows of gas, act to gravitationally stabilize the inner gas reservoirs.

Key words: molecular data – galaxies: kinematics and dynamics – galaxies: structure.

1 INTRODUCTION

Galactic bars are increasingly believed to be a critical stage in the secular evolution of disc galaxies in the present-day Universe (Masters et al. 2011; Chown et al. 2019; Géron et al. 2021, 2023). They provide an effective mechanism for the mass migration of molecular gas, which is driven inwards by the axi-asymmetric structure. This process is well understood and detailed in studies like Combes (1991), Bertin (2014), Sormani, Binney & Magorrian (2015), and Krumholz & Kruijssen (2015), which describe how bars exert powerful torques in host galaxies that drive gas onto resonant orbits with epicyclic frequencies commensurate with the pattern frequencies of the bars. This generally causes gas in outer-discs to fall inwards and results in the formation of resonant ring structures in the host galaxy, with the strongest resonances being at corotation and at the

Lindblad resonances (Shlosman, Frank & Begelman 1989; Combes 2001). Multiple direct observations of resonant ring structures using interferometry with high spatial resolutions support these models (e.g. Olsson et al. 2010; Topal et al. 2016; Davis et al. 2018; Lu et al. 2022). However, observational studies with measurements directly capturing the radial motions of gas, as opposed to measurements of its spatial distribution, are more sparse. This is largely due to the resolution and sensitivity required to accurately separate non-circular gas motions from the rotation of the gas disc. With data that meet these criteria, the presence of non-circular kinematics is often estimated by assuming velocity components are Gaussian, and fitting asymmetric profiles as a superposition of Gaussians (e.g. Lu et al. 2022), but can also be inferred more comprehensively by full three-dimensional (3D) kinematic modelling of the molecular gas (e.g. Lelli et al. 2022).

In reaction to the forcing frequencies of bars, simulations in the literature anticipate central starburst activity combined with quenching of the disc, resulting from the bulk inflow of molecular gas

★ E-mail: lucy.hogarth.18@ucl.ac.uk (LMH); a.saintonge@ucl.ac.uk (AS)

(e.g. Coelho & Gadotti 2011; Spinoso et al. 2017). Generally these simulations follow a 'compaction scenario' (Tacchella et al. 2016), whereby galaxies cycle through active and passive star-forming phases, regulated by inflows of molecular gas and subsequent outflows once intense star formation is triggered. Tacchella et al. (2016) find that galaxies at z ∼ 2 will oscillate along the main sequence on time-scales ≈ 0.4 t_H (where t_H is the Hubble Time). This scenario has also been simulated in the context of the Central Molecular Zone (CMZ) of a Milky Way-like galaxy by Krumholz & Kruijssen (2015). Their model predicts that the CMZ will cycle through phases above and below the star-forming main sequence on a time-scale of ∼ 17.5 Myr at resolutions of ≈ 100 pc. The short time-scales of star formation and quiescence in this model are also in agreement with the observational study conducted by Ellison et al. (2011), who measure elevated chemical abundances in the centres of low-mass barred galaxies. This indicates that these galaxies have experienced some past central enhancement in their star-formation rates, which was short-lived compared to the lifetime of their bars.

However, there is some contention between observational studies that have found that bars can both suppress and enhance the star-formation efficiencies (SFEs) of host galaxies. While multiple studies have confirmed elevated central molecular gas concentrations in barred galaxies (driven inwards by their forcing frequency at a rate faster than the gas is consumed; e.g. Sakamoto et al. 1999; Jogee, Scoville & Kenney 2005; Kuno et al. 2007; Yu et al. 2022), studies quantifying SFE are significantly more varied. Saintonge et al. (2012), for example, find no significant difference in the global SFEs of barred galaxies compared to a sample of un-barred galaxies. They acknowledge, however, that they may be averaging over galaxies undergoing different kinematic processes. This is reinforced by Jogee, Scoville & Kenney (2005), who suggest that SFEs of barred galaxies vary depending on the stage of their bar-driven gas inflow; that only galaxies hosting later-stage flows, once most molecular gas has been driven into the circumnuclear region, have enhanced SFEs. Studies such as Heitsch et al. (2006), Kruijssen et al. (2014), Davis et al. (2014), and Meidt et al. (2020), however, have shown that strong non-circular motions stabilize molecular clouds against collapse or disperse them entirely, especially in the dense circumnuclear regions of galaxies. In the context of bars, suppression of SFEs has been directly observed (e.g. Egusa et al. 2018; Maeda et al. 2020; Maeda 2023), but conversely, star-formation enhancement in bars and circumnuclear regions has also been reported (e.g. Watanabe et al. 2011; Wang et al. 2012; Salak et al. 2017), potentially reflecting the need to sub-divide barred galaxies based on their kinematic phase as suggested by Jogee, Scoville & Kenney (2005) and Saintonge et al. (2012).

In this study, we search for evidence of the effects bars have on the motion, distribution, and star-formation efficiency of molecular gas across a sample of nearby galaxies. More specifically, we seek to answer the following two questions:

(i) Can we find a statistical relationship between the presence of an optical bar and the detection of radial molecular gas motions?

(ii) How does the detection of non-circular molecular gas motions influence the SFEs of barred galaxies and their global properties?

By attempting to answer these questions, we aim to devise a method for identifying radial molecular gas flows in a sample of galaxies and to compare those radial flow detections to global galaxy properties (e.g. an optical bar). Furthermore, we want to address the conflicting conclusions in the literature as to whether a bar suppresses or enhances SFE in its host galaxy. We will address this by studying how ongoing radial gas motions impacts star-formation activity, and
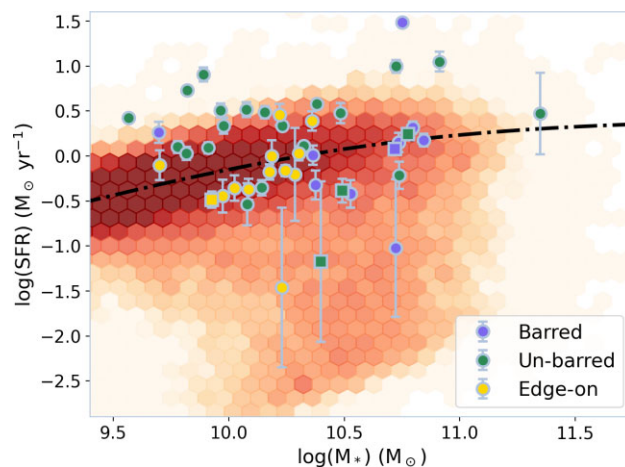

Figure 1. SFR–M_* plot illustrating the position of the ALMaQUEST sample with respect to the star-forming main sequence. SFRs are taken from the GSWLC-X2 catalogue (Salim et al. 2016; Salim, Boquien & Lee 2018) where available and stellar masses are taken from the NSA catalogue (Blanton & Roweis 2007; Blanton et al. 2011). The five objects not covered by GSWLC-X2 (square markers) are supplemented with SFRs from WISE (Wright et al. 2010). The GSWLC-X2 catalogue at $0.01 \leq z \leq 0.05$ is also illustrated in its entirety as a heat map and the star-forming main sequence (as derived by Saintonge & Catinella 2022) is indicated as a black dashed line. We colour the markers by the morphological class of the galaxy ('barred', 'un-barred' or 'edge-on'). Our classification procedure is detailed in Section 2.3.

how that relates to a galaxy's position on the star-forming main sequence.

Throughout this paper, we adopt a standard ΛCDM cosmology with $H_0 = 70$ km s^{-1} Mpc^{-1}, $\Omega_{m_0} = 0.3$, $\Omega_\Lambda = 0.7$ and a Chabrier (2003) IMF.

2 SAMPLE SELECTION & DATA

2.1 ALMaQUEST

The ALMA-MaNGA QUEnching and STar formation (AL-MaQUEST) sample (Lin et al. 2020; Ellison et al. 2024) consists of 47 galaxies selected from DR14 and DR15 of the Mapping Nearby Galaxies at Apache Point Observatory survey (MaNGA; Bundy et al. 2015), which span a wide range of specific star-formation rates and have stellar masses (M_*) in the range $10 \lesssim \log(M_*/M_\odot) \lesssim 11.5$ (including the green valley, main sequence and starburst regimes; see Fig. 1). The Atacama Large Millimeter Array (ALMA) ^{12}CO(1–0) (rest frequency 115.271 204 GHz) observations were collected from four individual ALMA programmes: 2015.1.01225.S, 2017.1.01093.S, 2018.1.00558.S (PI: Lin), and 2018.1.00541.S (PI: Ellison). We note that 1 object in the sample has no CO(1–0) detection.

All ALMA observations were taken in the C43-2 configuration (with a synthesized beam of 2.5 arcsec) to be comparable to the angular resolution of the optical integral-field spectroscopic data of the MaNGA survey. Typically, ALMaQUEST data are spatially resolved on physical scales ≈1.5 kpc (ranging between 0.9 to 6 kpc across the sample), with the largest structure the data are sensitive to being ≈14 kpc. The spectral set-up includes a high-resolution spectral window with a channel width of ≈10 km s^{-1} targeting ^{12}CO(1–0). The integration time per object ranges from 0.2 to 2.5 h to ensure a signal-to-noise ratio greater than 3 for more than 50 per cent

of the spatial pixels (spaxels) where the MaNGA Hα signal-to-noise ratio is also greater than 3.

In order to generate moment maps and calculate total H2 masses, we mask the ^{12}CO(1–0) data cubes by smoothing the original data cubes with Gaussian kernels with widths of $1.5 \times$ Bmaj$_{pix}$ spaxels spatially (where Bmaj$_{pix}$ is the width of the ALMA synthesized beam's major-axis in pixels) and 4 channels spectrally. Values lower than the standard deviation of the original data cube are set to 0 and all those above are set to 1. The original data cubes multiplied by these masks are what we use to calculate the total CO(1–0) luminosities (L$_{CO}$), with the relation:

$$L_{CO} = 3.25 \times 10^7 \times S_{CO}\Delta v \times \nu_{sys}^{-2} \times D_L^2 \times (1 + z)^{-3} , \quad (1)$$

where S$_{CO}$ is the total CO intensity obtained by summing over the masked cube, Δv is the channel width, ν_{sys} is the redshifted frequency of the CO(1–0) line, D$_L$ is the luminosity distance and z is the redshift of the object (obtained from the NASA–Sloan Atlas catalogue; NSA). The total molecular gas mass of each object is then calculated using the constant Galactic conversion factor $\alpha_{CO} = 4.3$ M$_\odot$ (K km s^{-1} pc^2)$^{-1}$, which includes a correction for the presence of heavier elements/molecules as detailed in Section 1. All galaxies in the sample have near-solar metallicities (calculated with the $12 + \log (O/H)$ proxy), with a median gas-phase metallicity of 8.69 ± 0.05, where we use the measurements of Lin et al. (2020) inferred with the O3N2 calibrator derived by Pettini & Pagel (2004).

2.2 Star-formation rates & stellar masses

2.2.1 MaNGA data products

As referred to in Section 2.1, the MaNGA survey (Bundy et al. 2015) is composed of integral-field spectroscopic (IFS) observations of galaxies in the local Universe ($z \lesssim 0.15$) with coverage from 3600 to 10 400 Å. We use optical emission line fluxes from the MaNGA PIPE3D pipeline derived from Data Release 17 (Sánchez et al. 2016, 2018; Sánchez et al. 2022). These are corrected for internal extinction by adopting an intrinsic H α/H $\beta = 2.86$ and a Milky Way extinction curve (Cardelli, Clayton & Mathis 1989). We follow the masking procedure detailed in Ellison et al. (2021), which makes restrictions on the optical spaxels used in their study combining MaNGA and ALMaQUEST data. This process can be summarized as follows:

(i) Spaxels are required to have S/N > 2 in H α, H β, [O III]λ5007 and [N II]λ6584 maps.

(ii) Each spaxel must fall in the star-forming portion of the Baldwin, Phillips, and Terlevich (BPT) diagram (Baldwin, Phillips & Terlevich 1981) using the Kauffmann et al. (2003) classification.

(iii) Spaxels require a H α equivalent width (EW) > 6 Å.

(iv) Using stellar-mass surface density maps (Σ_{M_*}) from the PIPE3D pipeline, each spaxel must have $\log \Sigma_{M_*} > 7$ (masking anomalously small values).

This procedure effectively masks low S/N spaxels and those contaminated by active galactic nuclei (AGN). We calculate star-formation rates (SFRs) from the extinction corrected, masked H α maps using the relation given in Kennicutt (1998), so that:

$$SFR [M_\odot yr^{-1}] = 7.9 \times 10^{-42} L(H\alpha) [ergs s^{-1}] , \quad (2)$$

where L(Hα) is the luminosity of H α emission. We note, however, that the masking process used to derive these SFR maps does significantly mask the central regions of some objects in the ALMaQUEST sample. In order to supplement MaNGA IFS therefore

we also utilize independent global star-formation rates (detailed in Sections 2.2.2 and 2.2.3).

2.2.2 GSWLC

The GALEX–SDSS–WISE Legacy Catalogue (GSWLC; Salim et al. 2016; Salim, Boquien & Lee 2018) contains measured properties of over 700 000 galaxies within the GALEX footprint and with Sloan Digital Sky Survey (SDSS) redshifts between 0.01 and 0.3. The catalogue is split into two versions: GSWLC-1 and GSWLC-2. We use SFRs from GSWLC-X2, which uses joint UV + optical + mid-infrared (IR) spectral energy distribution (SED) fitting, using Wide-field Infrared Survey Explorer (WISE) 22-micron photometry (see Section 2.2.3).

GSWLC-X2 covers 41 of the 46 objects we use from AL-MaQUEST, illustrated in Fig. 1 alongside the GSWLC-X2 catalogue at $0.01 \leq z \leq 0.05$.

2.2.3 WISE

For the remaining 5 objects from ALMaQUEST that are not included in the GSWLC-X2 catalogue, we use SFRs derived only from the WISE 22-micron photometry in the AllWISE data base (Wright et al. 2010; Cutri et al. 2021). We employ the method outlined in Janowiecki et al. (2017) to calculate SFRs from W4-band fluxes (SFR$_{W4}$), using SDSS redshifts to calculate the luminosities of the W1 and W4 bands and using the calibration of Jarrett et al. (2013) with a correction for stellar mid-infrared (MIR) contamination based on the W1-band luminosities:

$$SFR_{W4} [M_\odot y^{-1}] = 7.5 \times 10^{-10} \times (L_{W4} - 0.044 L_{W1}) [L_\odot] , \quad (3)$$

where L$_{W1}$ and L$_{W4}$ are the W1 and W4-band luminosities, respectively. We show the SFRs derived from WISE in Fig. 1 alongside those from the GSWLC-X2 catalogue.

2.2.4 NSA

For all of our objects, we use stellar masses calculated from K-corrected fits of Sersic fluxes from the NASA–Sloan Atlas (Blanton & Roweis 2007; Blanton et al. 2011). The NSA catalogue contains a wealth of parameters fit to photometry of local galaxies observed using SDSS. We use the parameter `nsa_sersic_mass` from the `drpall-v3_1_1.fits` file released with DR17 of SDSS.

2.3 Morphological sub-samples

For this investigation, we require a robust method for identifying barred galaxies within the sample. To achieve this, we use two catalogues that contain morphological data: Galaxy Zoo Data Release 2 (GZ2; Willett et al. 2013) and HyperLEDA (comprised of the HyperCat and Lyon–Meudon Extragalactic Data base/LEDA, henceforth referred to as HL; Makarov et al. 2014). We define three morphological sub-samples; barred, un-barred, and edge-on (where edge-on galaxies are too highly inclined to establish whether a bar is present). All galaxies in our sample are included in the HL data base, but 5 are missing from GZ2. The procedure we devised using GZ2 and HL is illustrated as a flowchart in Fig. 2.

For each galaxy in the sample, we first use GZ2 to determine whether the galaxy is edge-on (we use redshift debiased values from GZ2 throughout this procedure, as defined by Willett et al. 2013). We find using the GZ2 classifications of the edge-on sub-sample more
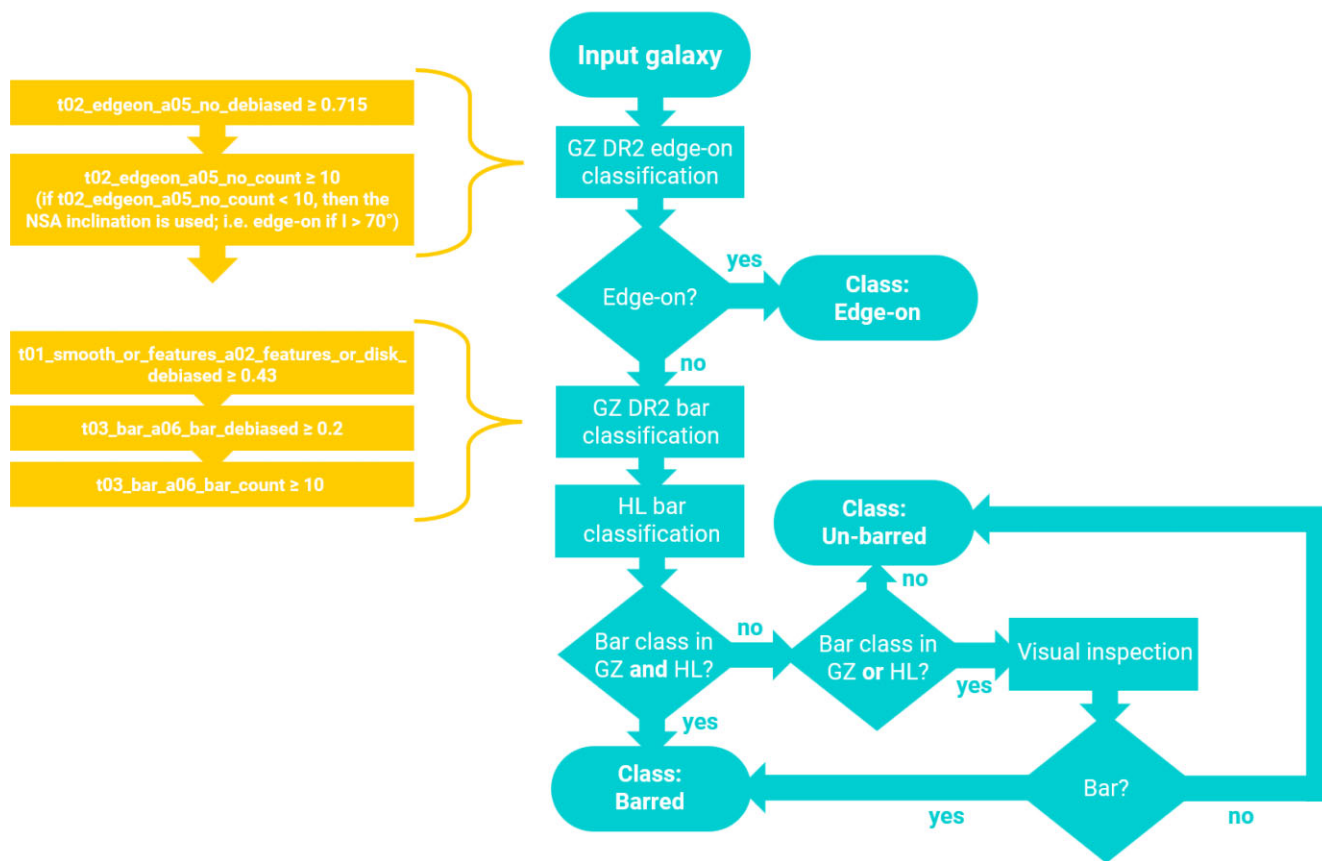
Figure 2. Flowchart illustrating our bar classification process using both GZ2 (Willett et al. 2013) and HL (Makarov et al. 2014).

accurate than using an inclination cut as the classification is based on whether the galaxy features are visible to the participants. Applying an arbitrary inclination cut led to some galaxies being classified as edge-on when their features were still discernible (e.g. a central bar was visible). Details of the combination of GZ2 parameters used in this classification are included in Fig. 2. We require a lower count threshold in the `t02_edgeon_a05_no_count` and `t03_bar_a06_bar_count` parameters than the recommendation (i.e. we use ≥ 10 instead of ≥ 20), as we find low count numbers for this parameter for many objects in the sample. However, after a visual assessment, we still find these classifications reliable with the lower count threshold. If the count number is <10 for the `t02_edgeon_a05_no_count`, we instead use an inclination cut of $>70°$ (where inclinations are taken from the NSA catalogue) to determine if a galaxy is edge-on. We also use the lower limit for `t03_bar_a06_bar_debiased` of ≥ 0.2, where Willett et al. (2013) find that ≤ 0.2 correlates strongly with galaxies classified as un-barred by the reference sources de Vaucouleurs et al. (1991) and Nair & Abraham (2010). Moreover, this lower limit is less biased towards strongly barred galaxies (i.e. it is more sensitive to weakly barred objects).

If a galaxy is not classed as edge-on, we look at whether it is classed as having a bar in both GZ2 and HL (details of the parameters used from GZ2 are given in Fig. 2). If GZ2 and HL both agree that the galaxy has a bar, it is added to our barred sub-sample. Likewise, if they both agree that the galaxy is un-barred, we add it to our un-barred sub-sample. If there is a disagreement between the catalogues (or it is only present in one of the catalogues), we visually inspect the SDSS

red–green–blue (RGB) image of the object and decide whether or not a bar is present. We note, however, that our classification procedure is contingent upon the visibility of features in SDSS imaging, which is dependent on both the redshift of galaxies and their size. Using redshift debiased classifications from GZ2 along with the lower-limit for bar classification should reduce this effect to some extent, but we are unable to discount it entirely given the imaging and studies available.

In total, 10 objects are included in the barred sub-sample, 23 in the un-barred sub-sample, and 13 in the edge-on sub-sample. These sub-samples are represented using SDSS *gri* composite images of the galaxies in Fig. 3. From this analysis, we calculate a bar fraction of 0.30 ± 0.08 (where the uncertainty is the binomial uncertainty), while the bar fraction calculated for the whole GZ2 sample in Willett et al. (2013) is 0.35 (given that we add the requirement of bar-detection in HL, a lower bar fraction is expected). Furthermore, the ALMaQUEST sample also covers a different range of global properties (M_*, SFR, size, etc.) compared to the full GZ2 sample. Our sub-samples are referred to as the 'morphological sub-samples' throughout the rest of this text.

3   RESULTS

3.1 Kinematic models

In order to create three-dimensional kinematic models of the sample, we use the process described in Hogarth, Saintonge & Davis (2023), which makes use of the KINematic Molecular Simulation tool
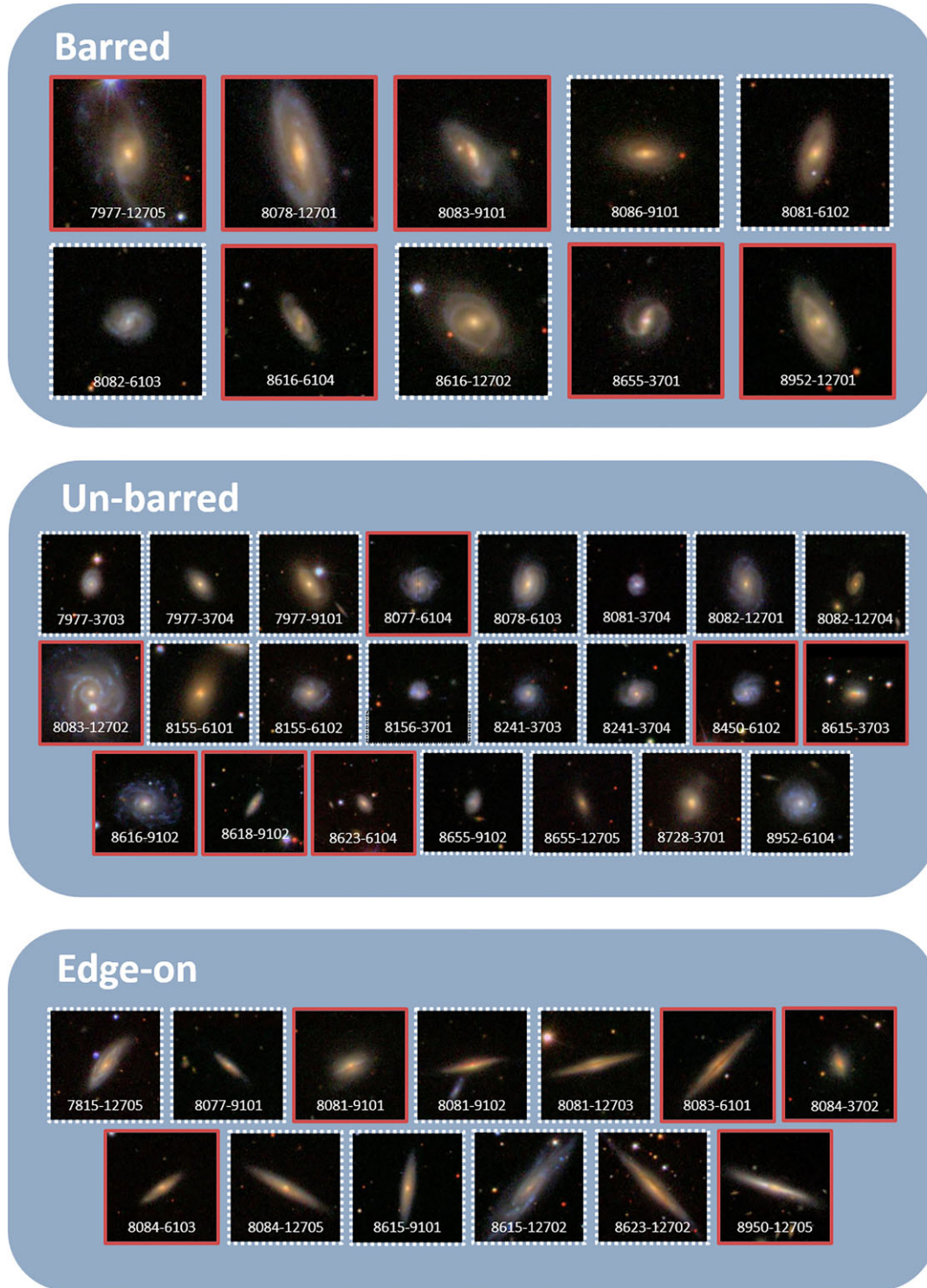
Figure 3. Optical SDSS *gri* composite images of the 46 galaxies in ALMaQUEST, grouped by their morphological classification as detailed in Fig. 2. Galaxies with a solid red border are classed as hosting radial bar-driven flows (those without have a dashed white border) by the process described in Fig. 4.

(KINMS; see Davis et al. 2013; Davis, Zabel & Dawson 2020; Lelli et al. 2022)[12]. KINMS allows us to create simple simulated interferometric data cubes by defining arbitrary surface brightness and velocity profiles. We also use the `KinMS_fitter`[3] wrapper of KINMS, which acts as a front end for the most common fitting tasks, and provides a simple interface for defining surface brightness and velocity profiles. It also provides an interface to the GASTIMATOR

[1]https://github.com/TimothyADavis/KinMSpy
[2]https://kinms.space

[3]https://github.com/TimothyADavis/KinMS_fit

package[4], which implements a PYTHON Markov chain Monte Carlo (MCMC) Gibbs sampler with adaptive stepping to fit the mock interferometric data cubes generated by KINMS, with predefined surface brightness and velocity profiles, to the original data cubes.

For each object in ALMaQUEST, we fit six different surface brightness profiles: an exponential disc, an exponential disc + central hole, a Gaussian ring, two exponential discs, an exponential disc + a Gaussian ring and two Gaussian rings (i.e. three single-component profiles and three double-component profiles). Each exponential disc has two free parameters describing the peak surface brightness ($F_{\mathrm{exp,\,peak}}$) and scale width (R_{exp}), while each Gaussian ring has three free parameters describing the peak surface brightness ($F_{\mathrm{gauss,\,peak}}$), the mean radius of the ring (R_{gauss}) and the width of the ring (σ_{gauss}). In order to reduce the number of parameters, in one-component profiles, the peak flux is fixed to 1 and in two-component profiles, the peak flux of the first component in fixed to 1, while the other is left to vary relative to the first. In addition, each model has three parameters describing the kinematic centre of the gas disc: the spatial coordinates of the dynamic centre (x_0, y_0) and the systemic velocity V_{sys}. Two further parameters, the position angle (PA) and inclination (i) are used to define the orientation of the disc. The total flux (F_{gas}) contained in the disc is also left to vary freely. In all of the models we use an arctan circular velocity curve to capture the gas rotation, which we find to be an excellent approximation of the molecular gas rotation for the majority of the objects. This profile requires two additional parameters: the maximum velocity (V_{max}) and the turnover radius (R_{turn}; the radius at which V_{max} occurs), so that the rotation velocity ($V_{\mathrm{rot}}(r)$) is described by:

$$V_{\mathrm{rot}}(r) = \frac{2 V_{\mathrm{max}}}{\pi} \arctan\left(\frac{r}{R_{\mathrm{turn}}}\right), \tag{4}$$

where r is the radius in the plane of the disc. The gas is also given a spatially constant velocity dispersion (σ_{gas}) in each model. The total number of parameters used in each model varies depending on the surface brightness model used, with 10 being the minimum and 14 the maximum.

In Fig. 4, we illustrate the process used to find the best-fitting model of each of the objects in the sample. Before fitting each model with MCMC, we fit an initial model using a least-squares minimization. The MCMC is set with uniform priors with physically motivated boundaries and run using 100 000 steps with 25 workers. Once a KINMS model has been fit using MCMC, we repeat steps 1–3 in Fig. 4 until all six predefined models have been generated and fit to the data. When all models have been fit to the input galaxy, we use the Bayesian Information Criteria (BIC) to select the best-fitting model out of the six KINMS models. The best-fitting model is the one that produces the lowest BIC, whereby more complex surface brightness models are penalized for larger parameter spaces:

$$\mathrm{BIC} \equiv k \log(n) - 2 \log(\widehat{L}), \tag{5}$$

where k is the number of parameters of the model, n is the number of spaxels in the data cube with signal and $\widehat{L}$ is the maximum value of the likelihood function defined in GASTIMATOR. We reject models that have fit parameters with uncertainties (defined as the width between the 16th and 84th percentiles of the probability distribution function) larger than half the size of the parameter range explored (we find that this works well as a method of rejecting unconverged models). We successfully find a converged best-fitting model for each object in the sample.

The next stage in our process is to add radial bar-driven flows to the best-fitting model (again using the same technique outlined in Hogarth, Saintonge & Davis 2023). We model radial motions induced by a central bar by using the `radial_barflow` function of the `KinMS_fitter` wrapper, which is based on the non-axisymmetric models described in Spekkens & Sellwood (2007). This radial bar-driven flow model simplifies the models outlined in Spekkens & Sellwood (2007) by assuming that there is a bar that extends from the galaxy's centre to a radius R_{b}, with a phase ϕ_{b}, and that the gas has constant radial and transverse velocities ($\overline{V}_{\mathrm{r}}$, $\overline{V}_{\mathrm{t}}$) within the bar's radius. $\overline{V}_{\mathrm{r}}$ represents the mean radial flow in the plane of the disc and $\overline{V}_{\mathrm{t}}$ the mean streaming speed of the gas perpendicular to $\overline{V}_{\mathrm{r}}$. The total radial flow velocity ($V_{\mathrm{f}}(r, \theta)$) is defined as:

$$V_{\mathrm{f}}(r, \theta) = \begin{cases} V_{\mathrm{f}}(\theta), & \text{if } r \leq R_{\mathrm{b}} \\ 0, & \text{if } r > R_{\mathrm{b}}, \end{cases} \tag{6}$$

where θ is the angle in the disc plane relative to the major-axis and $V_{\mathrm{f}}(\theta)$ is the flow velocity at radii $\leq R_{\mathrm{b}}$, which varies only with θ so that:

$$V_{\mathrm{f}}(\theta) = -\sin i [\overline{V}_{\mathrm{t}} \cos(2(\theta_{\mathrm{b}})) \cos\theta + \overline{V}_{\mathrm{r}} \sin(2(\theta_{\mathrm{b}})) \sin\theta], \tag{7}$$

where $\theta_{\mathrm{b}} = \theta - \phi_{\mathrm{b}}$ represents the angle relative to the position angle of the bar. This simplified radial bar-driven flow model is a first-order approximation of the non-circular kinematics of gas in the presence of a bar, where we assume that the bulk of the flow will happen in the circumnuclear region of the galaxy and that the flow in this region can be described with constant $\overline{V}_{\mathrm{t}}$ and $\overline{V}_{\mathrm{r}}$ (i.e. without a radial dependence). This reduces the computational time by reducing $V_{\mathrm{f}}(r, \theta) \rightarrow V_{\mathrm{f}}(\theta)$, and allows us to identify the presence of radial flows statistically over a sample of galaxies.

The radial bar-driven flow approximation adds an additional four parameters to our models. At minimum therefore each model has 14 free parameters and at maximum 18 free parameters. For each galaxy, we re-fit our best-fitting model with radial bar-flows using MCMC, using the same priors and set-up as described previously (with additional uniform priors for the radial flow parameters). If the model does not converge (based on the width of each parameter's uncertainty), we classify the object as not having a radial bar-driven flow. We also require either $\overline{V}_{\mathrm{t}}$ or $\overline{V}_{\mathrm{r}}$ to be larger than $2 \times$ the channel width (where $2 \times \Delta_{\mathrm{channel}} \approx 22$ km s^{-1}) as a threshold for radial flow detection. If these requirements are met, we recalculate the BIC using the new model in step 6 (see Fig. 4) and if BIC$_{\mathrm{w/\ radial\ flow}}$ < BIC$_{\mathrm{w/o\ radial\ flow}}$, the object is classed as having radial bar-driven flows (otherwise, it is classed as not having radial bar-driven flows). We note that in the majority of our barred objects classed as hosting radial bar-driven flows, we find a good alignment between the sky projection of ϕ_{b} and the optical position angle of the bar (echoing the results of López-Cobá et al. 2022, who find the same result using a more detailed bisymmetric flow model).

In Figs. 5, 6, and 7, we present examples of the models generated using the process detailed in Fig. 4. Fig. 5 illustrates the best-fitting model of the object with MaNGA Plate IFU 7977–9101 in our un-barred sub-sample, which is a Gaussian ring with no radial bar-driven flow component (in this case, we did not find a model with radial bar-driven flows with a converged solution). In Fig. 6, we show the models with and without radial bar-driven flows of object 8616–6104 in our barred sub-sample. This object has a more complex structure, and is best fit with a central exponential disc and outer Gaussian ring. Adding a radial bar-driven flow component also improves the fit to the data by lowering BIC$_{\mathrm{w/o\ flow}}$ = 4544 to BIC$_{\mathrm{w/\ flow}}$ = 4488. We overlay the spectrum of the model with radial bar-driven flows over
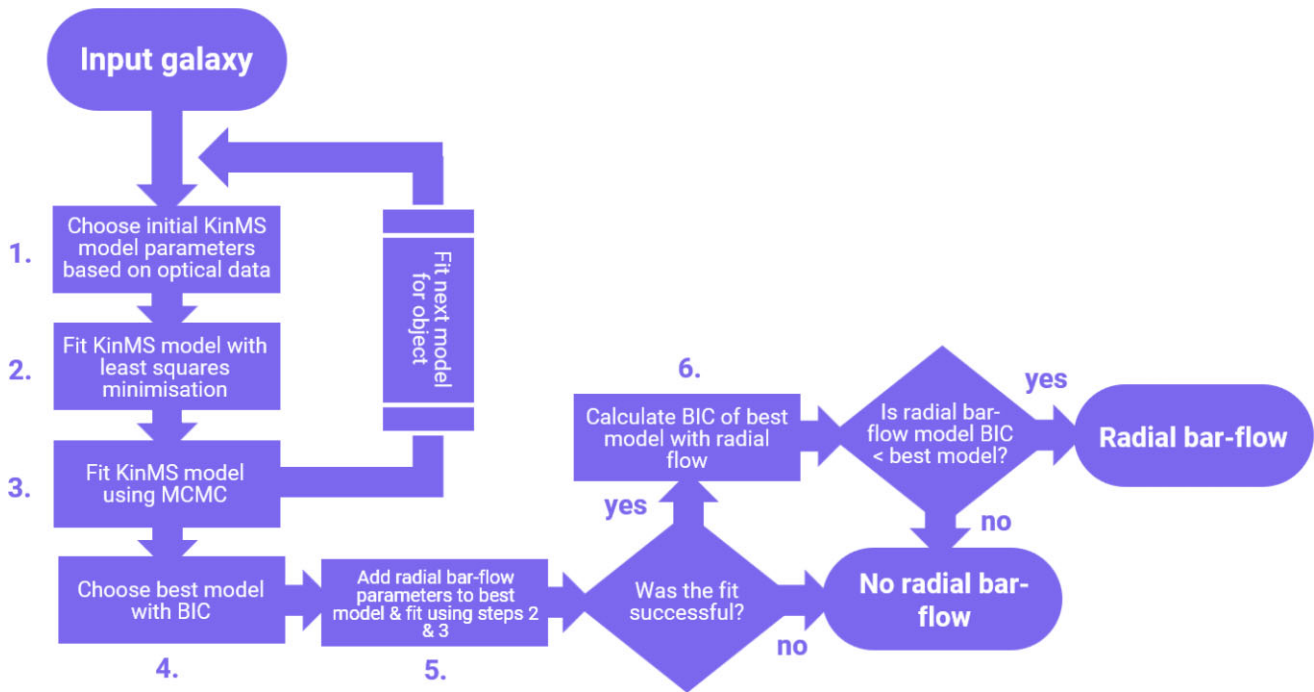
Figure 4. Flowchart illustrating our process for fitting and selecting the 'best-fitting' kinematic model for each of the galaxies in ALMaQUEST.
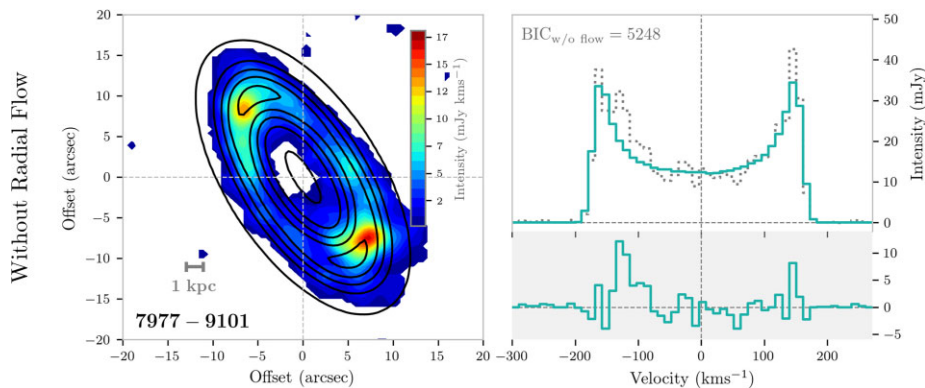

Figure 5. Example best-fitting model of the ALMaQUEST galaxy with MaNGA Plate IFU 7977–9101 in our un-barred morphological sub-sample. **Left**: masked zeroth-moment map of 7977–9101 with the best-fitting model overlaid in black contours. **Right**: spectrum extracted from the data cube of 7977–9101 (dotted grey line), with the spectrum extracted from the best-fitting model cube (solid turquoise line) overlaid. We also show the $BIC_{w/o\ flow}$ of the model above the spectra. The lower panel shows the residuals between the data and model spectra.

that of the model with no radial bar-driven flow in Fig. 6 to illustrate the improvement.

In Fig. 7, we present the position–velocity diagrams (PVDs) extracted from the models with and without radial bar-driven flows of object 8083–6101 in our edge-on sub-sample (we choose an edge-on object here as kinematic features are more easy to discern in objects that are more inclined). Again, the best-fitting model of this object is determined to be two Gaussian rings with radial bar-driven flows. Both the shape of the PVD extracted from the model and the residuals when compared to the data are improved by including radial bar-driven flows. In total, 19 objects in ALMaQUEST are classed as having radial bar-driven flows, which we will refer to as the 'radial-flow subset' for the remainder of this paper. This subset is also identified in Fig. 3.

3.2 Statistical presence of radial bar-driven flows

Our first question, as laid out in Section 1, requires us to determine whether we see a statistical relationship between the presence of an optical bar and the detection of non-circular kinematics like radial bar-driven flows. In Fig. 8, we show the proportion of galaxies in the radial bar-driven flow subset when divided into the morphological sub-samples. We find that $60\% \pm 15\%$ of the objects in the barred sub-sample are also in the radial bar-driven flow subset, compared to $30\% \pm 10\%$ and $38\% \pm 13\%$ of the un-barred and edge-on sub-samples, respectively. It can be assumed that the edge-on sub-sample is composed of both barred and un-barred galaxies, so a radial bar-driven flow proportion that falls between that of the barred and un-barred sub-samples is consistent. With our bar fraction of 0.30 ± 0.08, and given the radial bar-driven flow detection proportions of the barred and un-barred sub-samples, we would expect $\approx 39\%$ of the
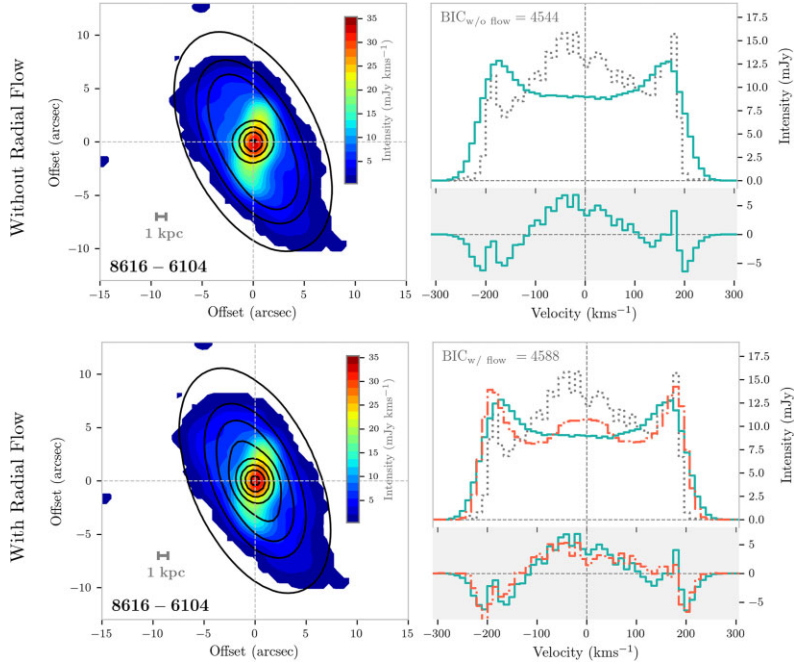
Figure 6. Example best-fitting models of the ALMaQUEST galaxy with MaNGA Plate IFU 8616–6104 in our barred morphological sub-sample, without (upper panels) and with (lower panels) radial bar-driven flows. The layout of the panels is equivalent to that in Fig. 5, except in the panel showing the spectra of the model with radial flows. In this panel, we plot the spectrum extracted from the model without radial flows (solid turquoise) and with radial flows (dashed red), to allow a visual comparison between the two. We show the BIC of both models above the spectra (i.e. $BIC_{w/o\ flow}$ and $BIC_{w/\ flow}$). In the case of this object, $BIC_{w/\ flow} < BIC_{w/o\ flow}$.
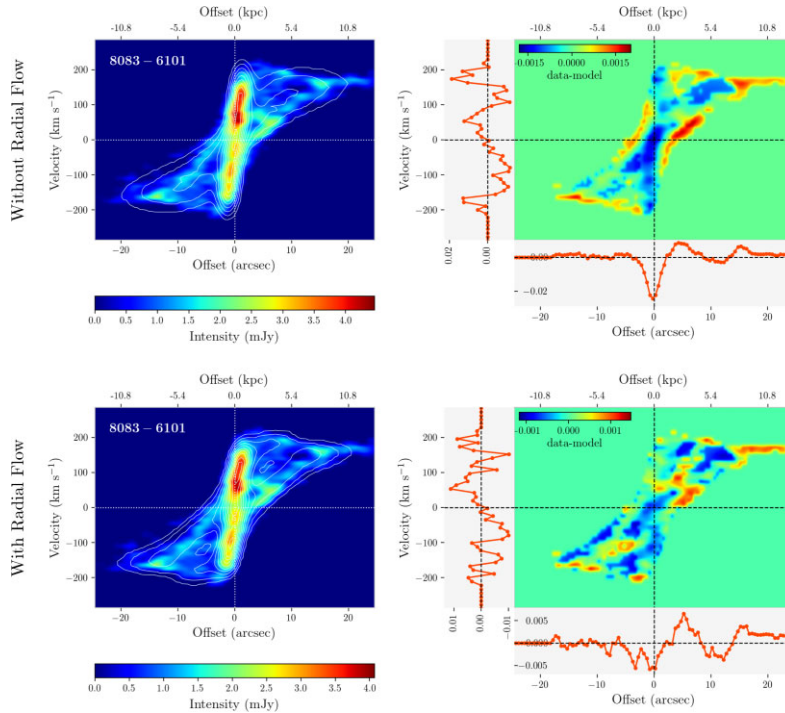
Figure 7. Example position–velocity diagrams (PVDs) illustrating the best-fitting models of the ALMaQUEST galaxy with MaNGA Plate IFU 8083–6101 in our edge-on morphological sub-sample, both without (upper panels) and with (lower panels) radial flows included in the models. **Left**: PVD extracted form the original data cube of 8083–6101 (heatmap) with the PVD extracted from the model overlaid as white contours. The kinematic centre (as determined by the model) is indicated by the white dashed line. **Right**: residual map calculated by subtracting the model PVD from the data PVD. One the left and bottom of this figure are the one-dimensional residuals created by summing over the residual map along the velocity and offset axes, respectively. The BIC of the model with radial bar-driven flows (lower row) is smaller than that of the model without radial bar-driven flows (upper row) for this object.
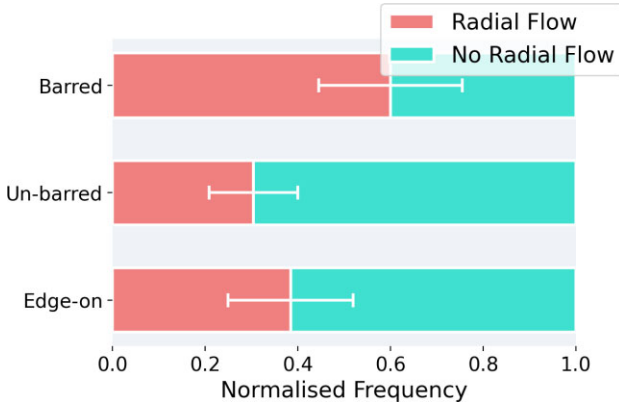
Figure 8. Bar plot representing the fraction of galaxies in each morphological sub-sample of ALMaQUEST that are determined to have radial bar-driven flows in their best-fit model. The frequency is normalized by the total number of galaxies in each sub-sample for ease of comparison. $60\% \pm 15\%$ of the barred sub-sample objects are determined to have radial bar-driven flows, compared to $30\% \pm 10\%$ and $38\% \pm 13\%$ of the un-barred and edge-on sub-sample galaxies, respectively. The error bars represent the uncertainty of the radial bar-driven flow fraction of each morphological sub-sample, assuming a binomial distribution.

edge-on sub-sample to be in the radial bar-driven flow subset, very close to our measured edge-on radial bar-driven flows fraction of $38\% \pm 13\%$. For completion, we demonstrate the effect of small number statistics in Fig. 8 by also showing the 1-sigma uncertainties of each morphological sub-sample, assuming a binomial distribution (i.e. uncertainty on each bar is $\sqrt{\left(p_{r,i}\ p_{nr,i} \right) / N_{morph,i}}$, where $N_{morph,\,i}$ are the numbers of objects in each morphological sub-sample i, $p_{r,\,i}$ are the radial bar-driven flow fractions and $p_{nr,\,i}$ are the no radial bar-driven flow fractions). Our predicted fraction of edge-on galaxies with radial bar-driven flows (i.e. calculated from the bar fraction) is well within the uncertainty of this morphological sub-sample. We also note that radial motions are more easily identified in galaxies with higher inclinations, as the component of the motions projected along the line of sight will be higher. This could potentially increase the radial bar-driven flow proportion of the edge-on sub-sample, however, given how close our predicted radial bar-driven flow fraction of the edge-on sample (inferred from the barred and un-barred sub-samples) is to our measured value, this effect does not appear to be significant.

In Fig. 9, we look at the proportion of galaxies that require a 1- or 2-component surface brightness model in their best-fitting KINMS model (see Section 3.1) for each morphological sub-sample. The top panel in the figure illustrates that the barred sub-sample is dominated by 2-component models ($90\% \pm 9\%$), more so than the un-barred and edge-on sub-samples ($30\% \pm 10\%$ and $69 \pm 13\%$, respectively). 2-component surface brightness models are generally associated with multiple gas rings, such as those caused by the forcing frequency of an axi-asymmetric feature like a bar. It follows therefore that our barred sub-sample would contain a high fraction of multiple-component models. We also anticipate that the fraction of barred sub-sample objects with multicomponent models would be greater than the fraction with radial bar-driven flows, as flows are transient while resonant structures exist for far longer timescales.

Using the objects in our radial bar-driven flow subset, in Fig. 10, we look at the distribution of the ratios of the radial velocity components ($\overline{V}_r$) and the transverse velocity components ($\overline{V}_t$) of the radial bar-driven flow models (see Section 3.1). If $\overline{V}_r / \overline{V}_t < 1$, the
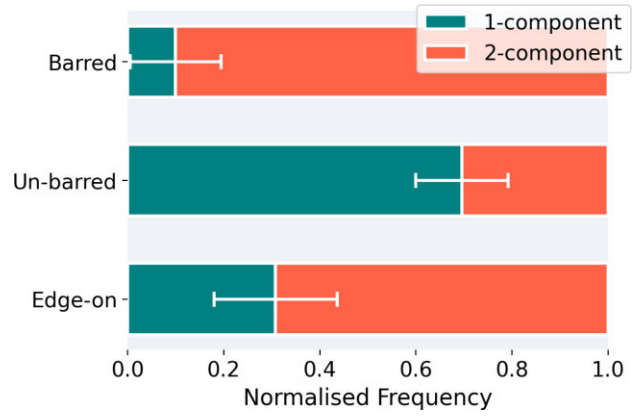

Figure 9. Bar plot representing the fraction of galaxies in each morphological sub-sample of ALMaQUEST that are determined to have a single-component (1-component) or double-component (2-component) surface brightness profile in their best-fitting model (see Section 3.1 for more details). The frequency is normalized to the total number of galaxies in each sub-sample for ease of comparison. $90\% \pm 9\%$ of the barred sub-sample objects are determined to have 2-component surface brightness models, compared to $30\% \pm 10\%$ and $69\% \pm 13\%$ of the un-barred and edge-on sub-sample galaxies, respectively. The error bars represent the uncertainty of the radial bar-driven flow fraction of each morphological sub-sample, assuming a binomial distribution.
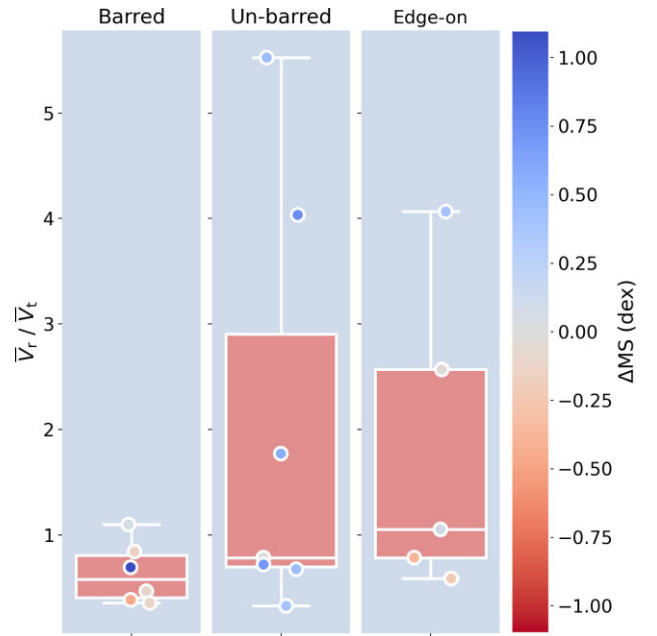

Figure 10. Distribution of the $\overline{V}_r / \overline{V}_t$ ratio (see the text for definition) of each of the morphological sub-samples. The median position, inner quartiles, and span of each distribution are shown by a box plot in each panel and the individual galaxies are shown as markers. The markers are colour-coded by their SFR offsets from the star-forming main sequence (ΔMS; defined in equation 8).

gas is more dominated by the transverse velocity component and therefore is spiraling inwards as opposed to if $\overline{V}_r / \overline{V}_t > 1$, which would indicate that the gas is moving more directly in the radial direction. In Fig. 10, we observe that the $\overline{V}_r / \overline{V}_t$ ratios of our barred sub-sample are all $\lesssim 1$, whereas, we see a greater spread of ratios in both the un-barred and edge-on sub-samples. This could imply that the un-barred and edge-on sub-samples contain objects undergoing

a range of dynamical processes driving the flows of molecular gas, as opposed to the barred sub-sample where we see more consistency. We can infer from this that there may be a similar kinematic process driving the flows of gas in the barred sub-sample (e.g. the forcing frequency of a bar).

3.3 Effect of radial bar-driven flows on the global SFEs of barred galaxies

Our second question posed in Section 1 involves investigating how non-circular molecular gas kinematics affects the global SFEs of barred galaxies. We define the SFE as the ratio of the total SFR (SFR_{tot}) and the total H2 gas mass ($M_{H2,tot}$). The SFR_{tot} we use are detailed in Sections 2.2.2 and 2.2.3 from the GSWLC-X2 and WISE catalogues, and we calculate $M_{H2,tot}$ using our masked ALMaQUEST $^{12}CO(1-0)$ data cubes (see Section 2.1).

In Fig. 11, we plot the distribution of $\log(SFE_{measured}[yr^{-1}])$ - $\log(SFE_{expected}[yr^{-1}])$, which estimates the enhancement/suppression of SFE relative to what would be expected given an object's location on the star-forming main sequence. $\log(SFE_{measured})$ are the SFEs we calculate with SFR_{tot} and $M_{H2,tot}$. $\log(SFE_{expected})$ is a function of the object's offset from the star-forming main sequence (ΔMS [dex]), which we define as:

$$\Delta MS \text{ [dex]} = \log\left(SFR_{tot} \left[M_{\odot} yr^{-1}\right]\right) \\ - \log\left(SFR_{MS}(M_*/M_{\odot}) \left[M_{\odot} yr^{-1}\right]\right) , \quad (8)$$

where $SFR_{MS}(M_*)$ is the star-forming main sequence as a function of stellar mass (M_*) using Saintonge & Catinella (2022) function, which is revised from the Saintonge et al. (2016) using M_* and SFRs from GSWLC-2:

$$\log\left(SFR_{MS}(M_*) \left[M_{\odot} yr^{-1}\right]\right) = 0.412 \\ - \log\left(1 + \left[\frac{10^{M_*/M_{\odot}}}{10^{10.59}}\right]^{-0.718}\right) . \quad (9)$$

We then derive $\log(SFE_{expected}(\Delta MS))$ by fitting a line to the $\Delta \log(SFE)$ illustrated in fig. 9 of Saintonge & Catinella (2022), with the form:

$$\log\left(SFE_{expected}(\Delta MS) \left[yr^{-1}\right]\right) = 0.29 \times \Delta MS + 0.04 + (-9.12) , \quad (10)$$

where -9.12 is the median $\log(SFE)$ of ALMaQUEST galaxies in the un-barred sub-sample that are within ± 0.3 dex of the star-forming main sequence (this aids interpretation of the relative offset between samples with respect to un-barred main-sequence galaxies). Any enhancement/suppression of SFE measured for our barred sub-sample galaxies therefore may purely be a consequence of their locations relative to the star-forming main sequence. Equally, the presence of a bar could be driving the position of a galaxy on the main sequence. For both scenarios, using $\log(SFE_{measured}) - \log(SFE_{expected})$ should reduce this effect.

In the left hand side panel of Fig. 11, we see an indication that the 'barred + radial flow' subset galaxies have generally suppressed SFEs, relative to both the 'barred + no radial flow' subset and un-barred sub-sample galaxies. We note that these subsets are small, particularly the 'barred + no radial flow' subset, so our analysis is once again limited by the small number of galaxies available in this work. However, we see a tenuous suggestion that the presence of radial flows in barred galaxies suppresses their SFEs relative to the 'barred + no radial flow' subset and un-barred sub-sample. In the right hand side panel of Fig. 11, we plot the un-barred sub-

sample alongside the 'barred + radial flow' and 'barred + no radial flow' subsets. We calculate the 2-sided Kolmogorov–Smirnov (KS) statistic for both radial flow barred subsets with the un-barred sub-sample and find that while the 'barred + no radial flow' subset is likely drawn from the same distribution as the un-barred sub-sample, the p-value of the 'barred + radial flow' subset is <0.05. This implies that we can reject the null-hypothesis at 2σ and the 'barred + radial flow' subset galaxies are likely drawn from a different distribution than that of the un-barred sub-sample.

Using SFR maps derived from H α emission from MaNGA, in Fig. 12, we plot the distributions of $SFE_{H\alpha,measured} - SFE_{expected}$ for the disc regions of the ALMaQUEST galaxies. We exclude the central region due to some objects (particularly, in the barred sub-sample) having this area masked due to AGN-contamination or low-S/N. With the SFR maps calculated using the method detailed in Section 2.2.1, we estimate the total disc SFR by summing spaxels in a circular annulus between 1 kpc and the r-band effective radius from the NSA catalogue for each object ($r_{50,r}$). M_{H2} spaxels then are summed in the same region and used to calculate $SFE_{H\alpha,measured}$. The $SFE_{expected}$ values used are the same as those derived in equations (8–10) using SFR_{tot} from GSWLC-X2 and WISE. We find a similar relative distribution between our morphological sub-samples as we observe in Fig. 11. Again, we are limited in particular when we interpret differences between the radial flow subsets in this figure due to the size of the samples, but we do see an indication that the median value of the 'barred + radial flow' distribution is suppressed relative to that of the 'barred + no radial flow' subset, which is approximately coincident with that of the un-barred sub-sample (although there is significant scatter). Using the same method as in Fig. 11, we use the 2-sided KS test to discern whether the SFE values from the radial bar-driven flows subsets in the barred sub-sample are drawn from the same distribution as the un-barred sub-sample. We find again that the p-value < 0.05 for the 'barred + radial flow' subset but >>0.05 for the 'barred + no radial flow' subset. This could imply that SFE is suppressed in the discs of galaxies in the 'barred + radial flow' subset relative to those in the un-barred sub-sample, which may contribute to the variations in global SFE distributions that we observe in Fig. 11. In our appendices (available as supplementary material), we also attempt to observe differences in $SFE_{H\alpha,measured} - SFE_{expected}$ between our morphological sub-samples and radial flow subsets in the central 1 kpc using median SFE spaxel values available in these regions.

We conduct a similar analysis to that carried out in Fig. 11, in Fig. 13, where we look at the distributions of concentration parameters of the objects in our three morphological sub-samples. The concentration parameter is defined as the half-light radius of the CO(1–0) intensity of each object, divided by $r_{50,r}$ (i.e. $r_{50,CO}/r_{50,r}$). In the left hand side panel of Fig. 13, we show the distribution of concentration parameters of each of the morphological sub-samples and the barred radial flow subsets. The objects in the 'barred + radial flow' subset all have $r_{50,CO}/r_{50,r} \lesssim 0.4$, whereas in the other morphological sub-samples there are broader distributions of concentration parameters. In the right hand side panel of Fig. 13, we compare the un-barred concentration parameter distributions with those of the barred sub-sample's radial flow subsets (in the same manner as the corresponding plot in Fig. 11). Again in this analysis, we find that the p-value of the distribution in the 'barred + radial flow' subset is < 0.05, suggesting we can reject the null hypothesis, while that for the 'barred + no radial flow' subset is >>0.05. This continues to suggest a similarity in the distributions of the 'barred + no radial flow' subset and un-barred sub-sample, with the 'barred + radial flow' subset appearing to be statistically distinct.
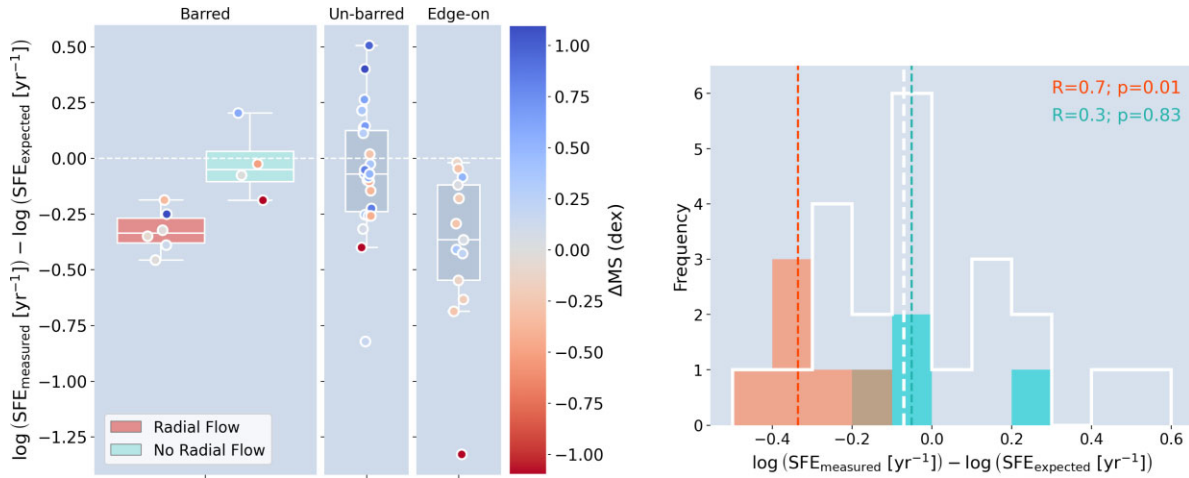
Figure 11. Distribution of the $SFE_{measured} - SFE_{expected}$ quantities (see the text for definition) of each of the morphological sub-samples. **Left**: the sample is divided into the three morphological sub-samples as in Fig. 10, and is split in the barred panel into the radial bar-driven flow and no radial bar-driven flow subsets. The median position, inner quartiles and span of each distribution are shown by a box plot in each panel and the individual galaxies are shown as markers. The markers are colour-coded by their SFR offsets from the star-forming main sequence (ΔMS). **Right**: histograms illustrating the $SFE_{measured} - SFE_{expected}$ quantity for the un-barred sub-sample (white histogram) and the 'barred + radial flow' and 'barred + no radial flow' subsets (red and turquoise histograms, respectively). The median position of each histogram is indicated by the white, red and turquoise dashed lines for the un-barred, 'barred + radial flow' and 'barred + no radial flow' distributions, respectively. The 2-sided KS statistic and p-value are listed in the plot to determine whether the 'barred + radial flow' and 'barred + no radial flow' distributions are potentially drawn from the same distribution as that of the un-barred sub-sample. The p-value of the 'barred + radial flow' subset suggests that we can reject the null hypothesis, but we note the low numbers in our statistical analysis.
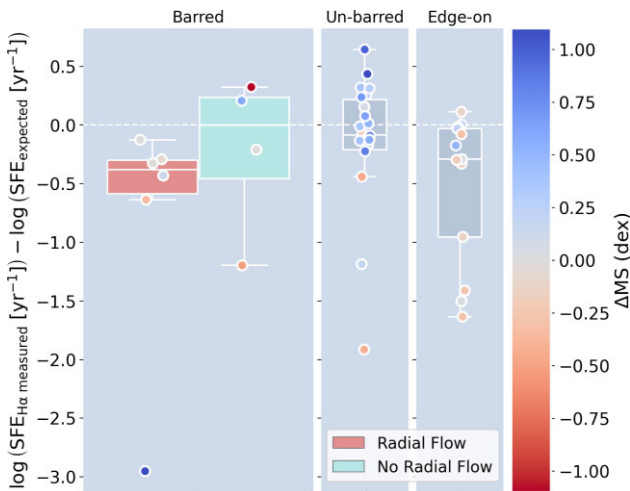

Figure 12. Distribution of the $SFE_{H\alpha,measured} - SFE_{expected}$ quantities (see the text for definition) in the disc regions of each of the morphological sub-samples, using H α emission from MaNGA. For each object, we sum SFR and M_{H2} spaxels within a circular annulus between 1 kpc and $r_{50,r}$ in order to estimate the total disc SFEs. The sample is divided into the three morphological sub-samples as in Fig. 11 and is split within the barred panel into radial bar-driven flow and no radial bar-driven flow subsets. The median position, inner quartiles, and span of each distribution are shown by a box plot in each panel and the individual galaxies are shown as markers. The markers are colour-coded by their SFR offsets from the star-forming main sequence (ΔMS).

As addressed in Section 2.2.1, spatially resolved analyses of SFRs in ALMaQUEST are limited by AGN contamination and/or low S/N in the central regions of some of the galaxies in the sample. However, in Figs. 14 and 15, we look at the molecular gas fraction and mass surface density within the central 1 kpc radius of each galaxy. In order to calculate the gas fractions ($\log M_{H2}/M_*$), we use the stellar-

mass surface density maps from MaNGA (see Section 2.2.1). Using the same method detailed previously, we calculate the 2-sided KS statistic of the central gas fractions of the 'barred + radial flow' and 'barred + no radial flow' subsets shown in Fig. 14 with those of the un-barred sub-sample. We find that the p-value in each case is >0.05, suggesting that both barred radial flow subsets have central gas fractions drawn from the same distribution as that of the un-barred sub-sample. Using the same analysis, in the left hand side panel of Fig. 15, we show the distribution of molecular gas mass surface densities ($\log \Sigma_{H2}$) of each of the morphological sub-samples. The median of the central molecular gas mass surface densities of the 'barred + radial flow' subset is clearly enhanced relative to that of the 'barred + no radial flow' subset and un-barred sub-sample. Using the 2-sided KS statistic, we find that the null hypothesis can be rejected for the 'barred + radial flow' subset, but not for the 'barred + no radial flow', when compared to the un-barred sub-sample. This may imply that the centres of galaxies hosting radial bar-driven flows are generally more gas-rich.

In Fig. 15, we consider whether the variations of S/N ratios of the ALMaQUEST molecular gas maps could explain the enhanced central molecular gas mass surface densities observed in the 'barred + radial flow' subset. We provide more detail of this process in our appendices (available as supplementary material), where we show that our results are robust against degrading all the original ALMaQUEST CO(1–0) data cubes to S/N < 30. The right hand side panel of Fig. 15 shows the molecular gas mass surface densities when all the ALMaQUEST data cubes have S/N < 30. The main difference in this panel is that one object changes subset from the 'barred + radial flow' subset to the 'barred + no radial flow' subset when we use KINMS to remodel the degraded data cubes. However, the median position of the central molecular gas mass surface densities from the 'barred + radial flow' subset remains higher than that of the 'barred + no radial flow' subset and the results from the 2-sided KS test remain consistent with those calculated in the left hand side panel.
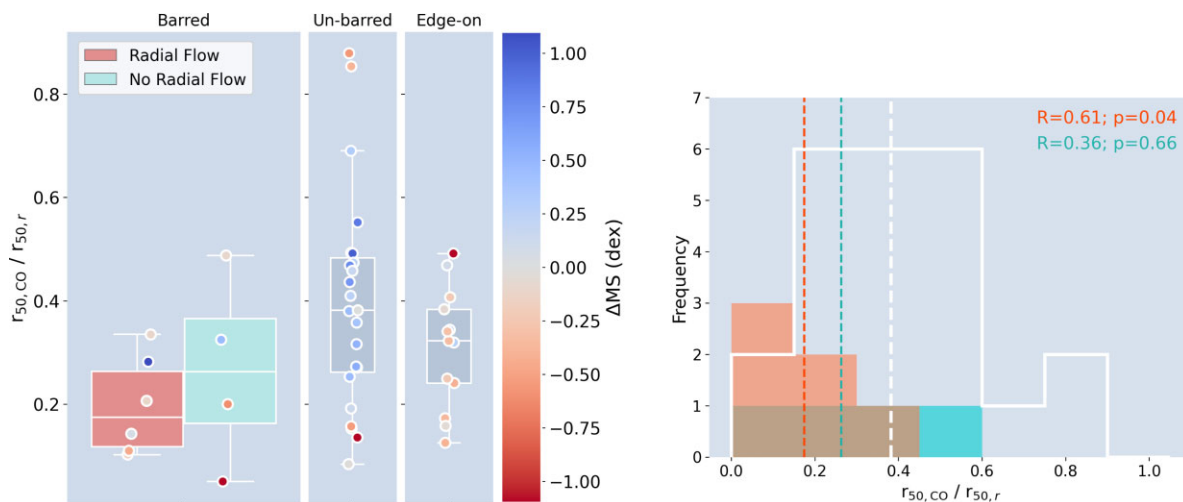
Figure 13. Distribution of the concentration parameters ($r_{50,CO}/r_{50,r}$ see the text for more details) of each of the morphological sub-samples. **Left**: the sample is divided into the three morphological sub-samples as in Figs. 10–12, and is split within the barred panel into the radial bar-driven-flow and no radial bar-driven flow subsets. The median position, inner quartiles and span of each distribution are shown by a box plot in each panel and the individual galaxies are shown as markers. The markers are colour-coded by their SFR offsets from the star-forming main sequence (ΔMS). **Right**: histograms illustrating the concentration parameters of the un-barred sub-sample (white histogram) and the 'barred + radial flow' and 'barred + no radial flow' subsets (red and turquoise histograms, respectively). The median position of each histogram is indicated by the white, red, and turquoise dashed lines for the un-barred, 'barred + radial flow' and 'barred + no radial flow' distributions, respectively. The 2-sided KS statistic and p-value are listed in the plot to determine whether the 'barred + radial flow' and 'barred + no radial flow' distributions are potentially drawn from the same distribution as that of the un-barred sub-sample. Both p-values suggest that we cannot reject the null hypothesis and that the 'barred + radial flow' subset is likely drawn from the same distribution as that of the un-barred sub-sample.
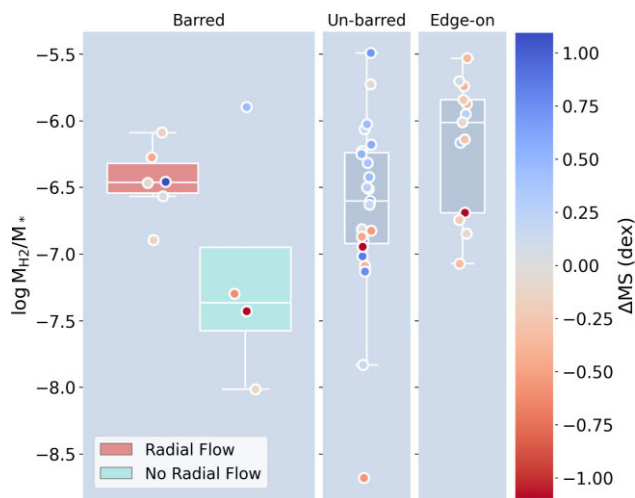

Figure 14. Distribution of the molecular gas fractions (M_{H2}/M_*) in the central 1 kpc radius of each of the morphological sub-samples, using stellar-mass maps from MaNGA (see Section 2.2.1). The sample is divided into the three morphological sub-samples as in Figs. 11–13 and is split within the barred panel into radial bar-driven flow and no radial bar-driven flow subsets. The median position, inner quartiles, and span of each distribution are shown by a box plot in each panel and the individual galaxies are shown as markers. The markers are colour-coded by their SFR offsets from the star-forming main sequence (ΔMS).

4 DISCUSSION

4.1 Features of radial bar-driven flows:

4.1.1 Barred galaxies

The primary question addressed in this work is whether there is a statistical relationship between the presence of an optical bar in a

galaxy and the detection of non-circular kinematics of molecular gas (with a focus on radial bar-driven flows). We find that $60\% \pm 15\%$ of galaxies in ALMaQUEST that we classify as barred (see Section 2.3 for details of the classification system) also host radial molecular gas flows (see Section 3.1 for our definition of radial bar-driven flows). This is in comparison to the $30\% \pm 10\%$ and $38\% \pm 13\%$ **of** the un-barred and edge-on sub-samples, respectively, which we illustrate in Fig. 8 (where the edge-on sub-sample is composed of both barred and un-barred galaxies). We can infer from this that barred galaxies are statistically more likely to possess non-circular molecular gas kinematics that resembles radial bar-driven flows (i.e. gas moving in the plane of a galaxy as the result of the forcing frequency of a bar; Spekkens & Sellwood 2007). This finding echoes numerical simulations of molecular gas transport in barred galaxies, such as those of Krumholz & Kruijssen (2015), where the role of large-scale galactic structures like bars are emphasized as critical drivers of gas dynamics and star formation at the centres of galaxies. However, Kruijssen et al. (2014) and Krumholz & Kruijssen (2015) also highlight the importance of time-scale when observing radial gas motions. Their models cycle through distinct phases of accumulation, starburst, outflow, and quenching, which results in a range of potential observations, depending on the phase in which a galaxy is observed. While radial bar-driven flows are more likely in our barred sub-sample galaxies, it also follows that it may not be present in all of our barred objects due to the impact of dynamical time-scales.

In addition to the greater likelihood of radial bar-driven flow detection in our barred sub-sample, we also find that $90\% \pm 9\%$ of these objects are best fit by a 2-component surface brightness model (instead of a 1-component model; see Section 3.1 for details on the modelling process). Our un-barred and edge-on sub-samples are significantly less likely to be best-fit by 2-component surface brightness models, with $30\% \pm 10\%$ and $69\% \pm 13\%$ preferring a 2-component model over a 1-component model, respectively (see Fig. 9). A multicomponent surface brightness model can indicate
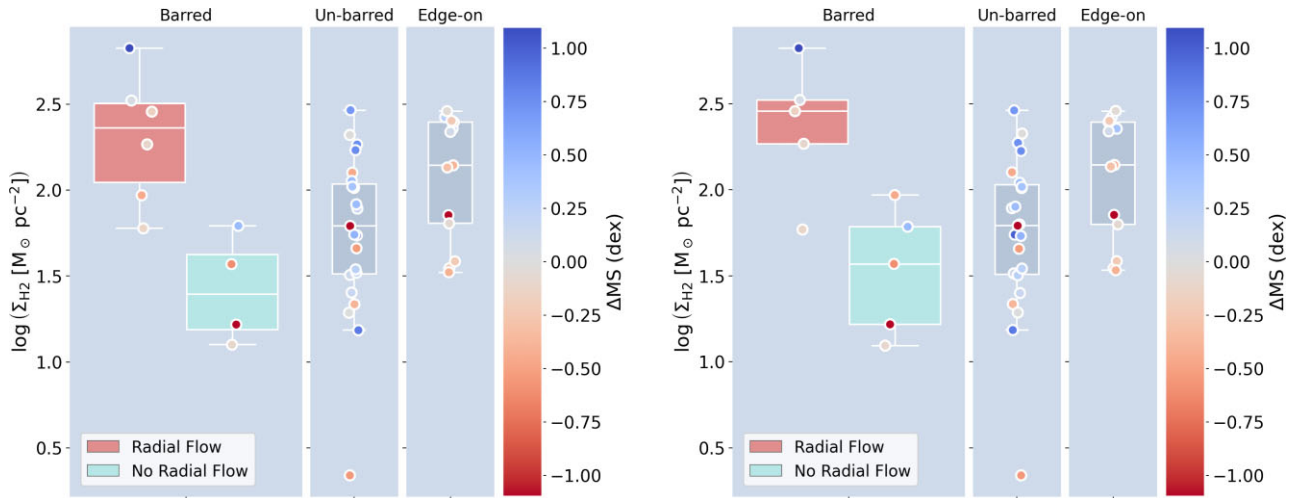
Figure 15. Distribution of the molecular gas mass surface densities (Σ_{H2}) in the central 1 kpc radius of each of the morphological sub-samples. **Left**: the sample is divided into the three morphological sub-samples as in Figs. 10–14, and is split within the barred panel into the radial bar-driven-flow and no radial bar-driven flow subsets. The median position, inner quartiles and span of each distribution are shown by a box plot in each panel and the individual galaxies are shown as markers. The markers are colour-coded by their SFR offsets from the star-forming main sequence (ΔMS). **Right**: as the left hand side panel, but using radial flow subsets defined once the ALMaQUEST cubes have been degraded to have S/N < 30 (see the text for detail).

the presence of a resonance system, where molecular gas is driven onto multiple resonant orbits by the pattern frequency of a bar or other axi-asymmetric feature (e.g. see Combes 1991; Comerón et al. 2014; Fraser-McKelvie et al. 2020; Chiba & Schönrich 2021). Strong resonant orbits occur at corotation and at the Lindblad resonances, where an orbit's epicyclic frequency is commensurate with the pattern frequency of the central bar. Molecular gas rings have been directly observed in multiple previous studies, including Lu et al. (2022), where the authors find evidence of a molecular gas inflow along the bar of the galaxy PGC34107, forming an asymmetric gas ring at the inner Lindblad resonance (ILR) using high-resolution millimeter interferometry from the Northern Extended Millimeter Array (NOEMA). We can infer therefore that a similar process may be underway in our barred sub-sample galaxies, whereby molecular gas is funneled along their bars into resonant orbits.

It is also noteworthy that the fraction of barred galaxies best-fit by 2-component surface brightness models is greater than the fraction in the 'barred + radial flow' subset. As considered in Section 3.2, this difference can be predicted from the literature, which generally points to radial bar-driven flows caused by bar instabilities being shorter lived than the lifetime of the bar itself. For example, Sormani et al. (2018) and Sormani & Barnes (2019) infer from their simulations of the CMZ that the intrinsic morphological asymmetry of a galactic bar leads to intrinsically transient and time variable gas inflows. Moreover, Schinnerer et al. (2023) study the inner 5 kpc of the local barred spiral galaxy NGC 1365 with the JWST/Mid-Infrared Instrument (JWST/MIRI) imaging alongside ALMA CO(2-1) mapping from PHANGS–ALMA (PHANGS: Physics at High Angular resolution in Nearby GalaxieS). They find asymmetric gas distributions along the 'bar lanes' (defined in Sormani et al. 2018, as the distributions of gas and dust along the leading sides of bars that extend out towards the disc) and a lopsided star-formation distribution, as well as evidence of streaming motions along the 'bar lanes'. Using hydrodynamical simulations, they are able to replicate these observations, with transient streaming motions that occur within a dynamical time (which in the case of NGC 1365 is ≈30 Myr, with streaming motion time-scales as small as ≈6 Myr). Largely, this is attributed to the clumpiness of the gas distribution,

which subsequently forms a highly variable inflow along the bar. Sormani et al. (2023) find very similar results when studying NGC 1097, which hosts cold gas inflow rates that vary over timescales of ≈10 Myr. Collectively, these studies strongly support a scenario of episodic gas accretion through short-lived radial inflows. When comparing these inflow time-scales to the lifetime of a bar, the literature suggests that a bar can be stable over a period of 1–10 Gyr (e.g. Shen & Sellwood 2004; Gadotti & de Souza 2006; Gadotti & Coelho 2015; Cavanagh et al. 2022). It follows therefore that the long lifetime of the bar would maintain resonant structures within a galaxy on time-scales that far exceed the lifetimes of transient radial flows. Consequently, it is more likely at any one time to observe a resonant gas structure than it is to observe a radial bar-driven flow in a barred galaxy, as we find in Section 3.2.

Another consistent property of the molecular gas in our barred sub-sample galaxies, especially the radial bar-driven flow subset, is low-concentration parameters (defined as $r_{50,CO}/r_{50,r}$ in Section 3.3 and illustrated in Fig. 13). We find a narrower range of concentration parameters for this subset of galaxies, at the low end of the distribution, suggesting that the gas in these objects is concentrated relative to that in the un-barred and edge-on sub-sample galaxies. The range of concentration parameters is also narrower than that measured for the objects in the barred sub-sample without radial bar-driven flow detection. However, the small size of this subset makes the comparison somewhat tenuous. This result is consistent with the findings of Yu et al. (2022), who use a sample of similar size drawn from EDGE–CALIFA (EDGE: Extragalactic Data base for Galaxy Evolution; CALIFA: Calar Alto Legacy Integral Field Area) to assess the correlation between central molecular gas concentration and large-scale galaxy asymmetry. In particular, the authors focus on the difference of gas concentrations between galaxies with and without an optical bar, but do not find a statistically significant difference between the concentration parameters they calculate for these two sub-samples. This is despite the fact that their barred distribution peaks at higher gas concentrations than their un-barred distribution. Our results illustrated in Fig. 13 support a similar scenario, where the concentration parameters of our barred sub-sample galaxies do peak at a lower value than the distribution drawn from the un-barred and

edge-on sub-samples (although they are not drawn from a different distribution according to the 2-sided KS statistic). Ultimately, more data are required to assess this result, but in the context of the high fraction of resonant gas structures found in our barred sub-sample, it follows that this gas would be more centrally concentrated along inner orbits (e.g. Sakamoto et al. 1999; Jogee, Scoville & Kenney 2005; Kuno et al. 2007; Combes et al. 2014).

We also find a notable consistency in some of the dynamical properties of the radial bar-driven flow subset of our barred sub-sample. In Fig. 10, we show that all the objects in our 'barred + radial flow' subset have a ratio of radial to transverse velocities ($\overline{V}_r / \overline{V}_t$) $\lesssim$ 1 (see Section 3.2 for more details). This is in comparison to both the un-barred and edge-on radial bar-driven flow subsets, which have a larger scatter of $\overline{V}_r / \overline{V}_t$. $\overline{V}_r / \overline{V}_t << 1$ suggests essentially circular orbits, while $\overline{V}_r / \overline{V}_t >> 1$ implies significant non-circular motions. Spekkens & Sellwood (2007) also comment on the relevance of the $\overline{V}_r / \overline{V}_t$ ratio, finding that their bisymmetric model produces $\overline{V}_r / \overline{V}_t = 1$ for solid-body rotation and $\overline{V}_r / \overline{V}_t \approx 0.67$ for flat rotation. All of the objects in our 'barred + radial flow' subset have $R_b > R_{turn}$, meaning that their bars extend beyond the rising portion of their rotation curves (i.e. where there is roughly solid-body rotation). As our $\overline{V}_r$ and $\overline{V}_t$ parameters are spatially constant in the region up to R_b, we are effectively averaging these velocities over the rising and flat portions of the rotation curves. Values of $\overline{V}_r / \overline{V}_t \lesssim 1$ for our 'barred + radial flow' subset appear therefore to be in the range anticipated by Spekkens & Sellwood (2007) for distortions created by the presence of a bar. It is, however, possible that our radial bar-driven flow model is capturing shocks induced along molecular ridges (i.e. long structures along the leading edges of a bar) in our barred sub-sample, which can rapidly decelerate molecular gas and potentially alter our $\overline{V}_r$ and $\overline{V}_t$ parameters (e.g. Kuno et al. 2000). In the case of our un-barred and edge-on sub-samples, for which $\overline{V}_r / \overline{V}_t >> 1$, the measurements are outside the values anticipated by Spekkens & Sellwood (2007), reinforcing our argument that the flows in these objects are, at least in part, kinematically distinct from those in the barred sub-sample.

The transverse velocity component of a bar flow should not in principle be related to the circular velocity resulting from the stellar potential. We investigate this in Fig. 16, where we show that there is no statistically significant correlation (p-values >>0.05) between the transverse velocity components and either the total stellar masses or circular velocities of our sample galaxies. Our measured transverse velocity components therefore do not seem connected to the stellar potentials and can be viewed as distinct features of the gas flows of our objects. This result once again implies that there is a kinematic similarity in how cold gas is moving in our barred sub-sample galaxies, compounding the evidence that they are undergoing the same process, drawing gas onto resonant orbits due to the forcing frequencies of the bars. While it is not possible to distinguish between gas inflows and outflows in the plane of the discs using our bisymmetric radial bar-driven flow model, given the enhanced central molecular gas mass surface densities of our 'barred + radial flow' subset galaxies, the preponderance of resonant inner orbits in these objects and our comparisons to the literature in this discussion, we are inclined to infer that we are observing radial bar-driven inflows as opposed to outflows.

4.1.2 Un-barred galaxies

While the focus of this paper is the molecular gas kinematics of galaxies hosting an optical bar, we also find some compelling
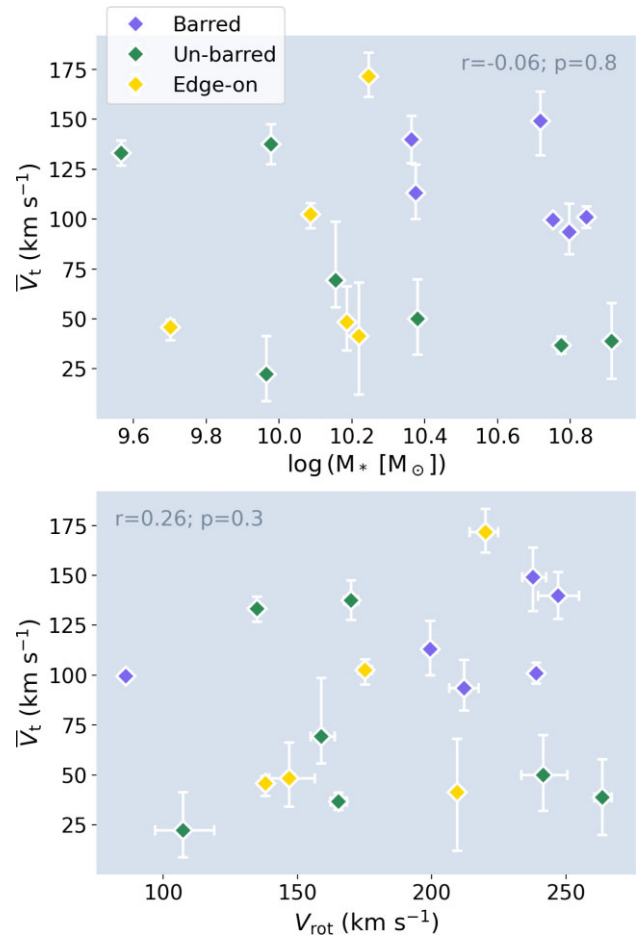

Figure 16. Dependence of the transverse velocity components ($\overline{V}_t$) of our radial flow subsets. **Top**: plot of $\overline{V}_t$ against M_*. The Spearman correlation coefficient r = −0.06 and the p-value >> 0.05. These quantities are therefore not correlated. **Bottom**: plot of $\overline{V}_t$ against the circular velocity (V_{rot}). The Spearman correlation coefficient r = 0.26 and the p-value >> 0.05, again suggesting there is no correlation between these quantities.

results for our un-barred sub-sample. Only 30% ± 10% of un-barred galaxies are best modelled with radial bar-driven flows and the majority only require a 1-component surface brightness profile to describe the spatial distribution of their molecular gas (70% ± 10%; see Section 3.2). When comparing these findings with those from the barred sub-sample, we can infer that these objects are kinematically distinct. Moreover, the results from Fig. 13 further support this inference by illustrating the wide range of concentration parameters in the un-barred sub-sample and the higher median of the distribution. Once again, we can defer to Yu et al. (2022) for a potential explanation for the wide range of concentration parameters that we measure. The authors find a correlation between the strength of non-axisymmetric structures and central molecular gas concentration, where axi-asymmetric structures can be due to a bar or the presence of spiral arms. They suggest that instead of there being a distinct difference between the gas dynamics in barred and un-barred galaxies, that the dynamics are a function of asymmetry, with a unified mechanism. This is further supported by Géron et al. (2021, 2023), who extend this idea to different bar types, suggesting that there is a continuum of bar types, more specifically that there is no bifurcation between weak and strong bar in terms of the effects on their host galaxies. Our un-barred sub-sample likely contains galaxies

with a range of structural asymmetries, corresponding to a range of pattern strengths with which to drive gas inwards. Géron et al. (2021, 2023) and Walmsley et al. (2022) also note that weak bars are underdetected in GZ2, with the barred sub-sample preferring strong bars. While our barred sub-sample is dominated by strong bars, the un-barred sub-sample is likely to contain a fraction of weakly barred galaxies. It is also possible that the un-barred sub-sample (as well as the other morphological sub-samples) contains galaxies under-going minor mergers or interactions, which can also act to centralize the molecular gas distributions (e.g. Eliche-Moral et al. 2011).

4.2 Do radial bar-driven flows affect the SFEs of barred galaxies?

In Section 3.3, we investigate the second goal of this paper, which is to look for correlations between non-circular gas kinematics and the SFEs of galaxies in our barred sub-sample. We define the quantity $\log(\mathrm{SFE_{measured}}) - \log(\mathrm{SFE_{expected}})$ (see Section 3.3 for a detailed definition) to measure the enhancement/suppression of a galaxy's global SFE relative to the offset of SFE expected given its location on the star-forming main sequence (and the median global SFE of ALMaQUEST objects in the un-barred sub-sample within the scatter of the main sequence). In Fig. 11, we illustrate the distribution of this quantity for each of our morphological sub-samples and radial flow subsets. Notably, we see an indication that the SFEs of the 'barred + radial flow' subset galaxies are suppressed relative to the those of the un-barred sub-sample and 'barred + no radial flow' subset galaxies. This result could imply that our 'barred + radial flow' subset galaxies have suppressed total SFEs relative to those expected from their positions with respect to the star-forming main sequence. Echoing the distributions in Fig. 13, we also see a broader range of SFE offsets in the un-barred sub-sample, which could again be explained by the likelihood that this sub-sample is composed of a variety of galaxy morphologies, as argued in Section 4.1.2. In order to investigate Fig. 11 further, in Fig. 12, we plot the distributions of $\log(\mathrm{SFE_{H\alpha,measured}}) - \log(\mathrm{SFE_{expected}})$ calculated in the discs of each of our morphological sub-sample galaxies, derived from MaNGA optical IFS (see Section 2.2.1). We find a similar distribution to that of Fig. 11 in terms of the relative enhancement/suppression between the morphological sub-samples and radial flow subsets. Again, our interpretation of this result is limited by the size of the samples, but finding a comparable result by an independent method does add credence to our interpretation of SFE suppression of the 'barred + radial flow' subset galaxies. Extending this interpretation with Fig. 12, the suppression of SFE within the disc regions of galaxies in the 'barred + radial flow' subset could be seen, in the context of the 'Compaction Scenario' (Tacchella et al. 2016), as evidence of the disc being quenched by the inward radial flow of molecular gas. However, larger-scale analysis dividing barred galaxies into subsets depending on radial bar-driven flow detection is required to substantiate this argument.

In the literature, there is a general link between a galaxy being quenched and it having a higher stellar mass surface density (Σ_{M_*}) in its central 1 kpc radius (e.g. Fang et al. 2013; Woo et al. 2015; Davis et al. 2022). We assess this connection in Fig. 17 and find that our barred sub-sample has a higher median central Σ_{M_*} than those of the other morphological sub-samples. Furthermore, all of the galaxies in the 'barred + radial flow' subset have central Σ_{M_*} larger than $\approx 8.25\ \mathrm{M_\odot\ pc^{-2}}$, whereas the un-barred and edge-on sub-samples, as well as the 'barred + no radial flow' subset, contain galaxies that have stellar mass surface densities below that threshold. Once again, this suggests a similarity within the 'barred + radial flow' subset.

It also is consistent with the literature, given that our most SFE-suppressed subset also has consistently high central Σ_{M_*}, suggesting that growth of the central stellar mass surface density may be a signal of galactic quenching.

It is widely theorized that molecular gas is depleted or expelled after large-scale starburst activity and exhausted in bulge-dominated early-type galaxies (e.g. Gavazzi et al. 2015; Zolotov et al. 2015; Tacchella et al. 2016; Spinoso et al. 2017). However, in Davis et al. (2014, 2016) and French et al. (2015), this scenario is contradicted, the authors finding higher than expected gas fractions ($\log M_{H2}/M_*$) in early-type galaxies. Furthermore, Lin et al. (2022) report in their analysis of green valley galaxies in ALMaQUEST that quenching is driven by the combination of reduced $\log M_{H2}/M_*$ and suppressed SFE, challenging the picture that star formation is quenched purely by gas depletion. In Fig. 14, we look at the distribution of molecular gas fractions in a 1 kpc central aperture of each of the morphological sub-samples. The 'barred + radial flow' subset galaxies, despite having suppressed SFEs, do not appear to have depleted central molecular gas reservoirs, with the median central molecular gas fraction for the 'barred + radial flow' subset galaxies roughly the same as that of the un-barred sub-sample galaxies (and enhanced compared to that of the 'barred + no radial flow' subset galaxies). We conduct the same analysis using total molecular gas fractions and find a similar result. Moreover, in Fig. 15, we measure a higher median central molecular gas mass surface density in the 'barred + radial flow' subset, consistent with Fig. 13 (i.e. in agreement with their centralized gas distributions). Using the 2-sided KS statistic, we find that the central molecular gas mass densities of the 'barred + radial flow' subset galaxies are potentially drawn from a different distribution than those of the un-barred sub-sample (i.e. p-value < 0.05). Visually, it appears that the 'barred + radial flow' subset galaxies are drawn from the higher-density end of the un-barred sub-sample's Σ_{H2} distribution and the 'barred + no radial flow' subset from the lower-density end. We can infer from the higher median central molecular gas mass surface densities of the 'barred + radial flow' subset galaxies that molecular gas depletion is not the main driver of SFR suppression of our 'barred + radial flow' subset. This result is also supported by Fig. 12, with which we tentatively argue that the suppressed median disc SFEs in the 'barred + radial flow' subset galaxies could be caused by inward radial bar-driven flows drawing gas away from their discs and effectively quenching star formation. Radial bar-driven flows of molecular gas appear to centralize the gas reservoirs of these objects, but do not fuel enhancements in SFR (i.e. neither globally or in the discs; we conduct a similar analysis for the central 1 kpc in our appendices – available as supplementary material). In our un-barred sub-sample, however, the galaxies with similarly high central molecular gas mass surface densities have significantly higher ΔMS than those in the 'barred + radial flow' subset. This supports the argument that the presence of a bar is responsible for the SFE suppression instead of central gas depletion in these objects.

In order to explain the apparent relative suppression of SFEs in our 'barred + radial flow' subset galaxies, we may require a more dynamical prescription of quenching. Dynamically driven shear and the stability of the central gas reservoirs against collapse contribute to a morphological picture of quenching ('morphological quenching'; Martig et al. 2009). For example, Davis et al. (2014) and Gensior, Kruijssen & Keller (2020) discuss the role of gas dynamics on SFE suppression in early-type galaxies (ETGs), in which the majority of the molecular gas reservoirs are concentrated in the rising portions of the galaxies' rotation curves, where shear is generally higher. Although our barred sub-sample galaxies are clearly morphologically
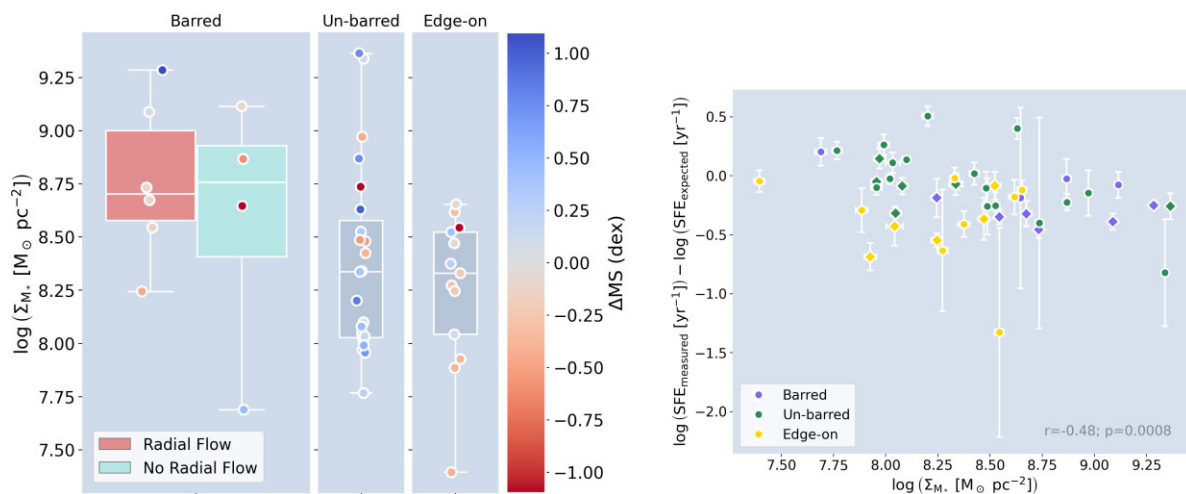
Figure 17. Distribution of the stellar mass surface densities (Σ_{M_*}) in the central 1 kpc radius of of each of the morphological sub-samples. **Left**: the sample is divided into the three morphological sub-samples as in Figs. 10–15 and is split within the barred panel into radial bar-driven flow and no radial bar-driven flow subsets. The median position, inner quartiles, and span of each distribution are shown by a box plot in each panel and the individual galaxies are shown as markers. The markers are colour-coded by their SFR offsets from the star-forming main sequence (ΔMS). **Right**: relationship between $\log(\text{SFE}_{\text{measured}}) - \log(\text{SFE}_{\text{expected}})$ and central stellar mass surface density. Each marker is colour-coded by morphological sub-sample. Objects in the radial bar-driven flow subset are illustrated with a diamond-shaped marker. The Spearman correlation coefficient r $= -0.48$ and the p-value $<< 0.05$, suggesting our $\log(\text{SFE}_{\text{measured}}) - \log(\text{SFE}_{\text{expected}})$ quantities and the central stellar mass surface densities are negatively correlated.

distinct from ETGs, the 'barred + radial flow' subset does contain consistently centralized molecular gas reservoirs, implying that the gas is restricted to the high-shear regions of the host galaxies. Furthermore, the presence of radial flows will also contribute to shear, particularly in the central areas where most of the gas is concentrated. The presence of strong shear could also increase the velocity dispersion of cold gas clouds by actively pulling them apart, increasing the Toomre Q parameter (Toomre 1964). This is corroborated by the studies of M51 by Meidt et al. (2012, 2013), who detect a clear anticorrelation between strong gas flows and star formation (traced by H α and 24 μm emission). This implies a direct connection between the star-forming ability of giant molecular clouds (GMCs) and their dynamical environment, suggesting that GMCs in the vicinity of radial streaming motions are significantly stabilised against gravitational collapse. These findings contribute to a scenario where our 'barred + radial flow' galaxies have driven gas inwards (via the radial flows induced by bars) towards central molecular gas reservoirs that are largely gravitationally stable. This is in comparison to our 'barred + no radial flow' subset galaxies, which are less centrally concentrated and obviously do not have the contribution to shear provided by radial flows. As discussed in Section 4.1.1, these objects are potentially at different dynamical stages of their evolution (e.g. prior to the radial inflow of gas or after a central starburst once the central molecular gas reservoir gravitationally destabilizes). As depicted in Figs. 11 and 13, our most concentrated objects are largely quenched, with SF restricted to the central regions and maybe also subject to dynamical suppression.

While there are multiple studies in the literature that find a connection between galaxies hosting bulges and SFE suppression (e.g. Saintonge et al. 2012; Martig et al. 2013; Davis et al. 2014), the influence of bars on the star-forming potential of galaxies is less consistent. Wang et al. (2012) summarize the variety of results in this field, finding that the galaxies in their sample with strong bars either have enhanced central star-formation rates or star formation that is suppressed. Resolved studies find that the SFE can vary along a bar and between galaxies; e.g. Maeda et al. (2023) find star formation

generally suppressed along bars but enhanced at the bar ends, while Díaz-García et al. (2021) find no evidence of SFE variation between the bar and bar ends but significant variation between galaxies. These differences may be explained to some extent by bar/bar-end definitions in the case of resolved studies, but the variety of results may also indicate that galaxies classed as barred in these studies contain a mixture of objects dominated by different mechanisms or at different stages of their evolution. Our identification of radial bar-driven flows may provide a method to sub-divide barred galaxies into subsets with similar global properties based on the large-scale dynamics of their molecular gas. We suggest that this sub-division of optically barred galaxies potentially captures the portion of objects with suppressed SFEs in the literature. Without making the distinction, many studies find little difference in the star-formation efficiency of barred galaxies when comparing them to their un-barred counterparts (e.g. Saintonge et al. 2012). To assess this result further, a larger sample of galaxies with CO data of comparable resolution and sensitivity to the data of ALMaQUEST would be required.

5 SUMMARY & CONCLUSIONS

In this work, we investigate the statistical relationship between the presence of an optical bar and radial molecular gas flows and, furthermore, whether that connection influences the star-formation activities of the host galaxies. We use CO(1–0) maps of 46 galaxies from the ALMaQUEST survey to create 3D kinematic models (using the KINMS package), from which we infer whether or not there is evidence of radial gas motions. In tandem with our dynamical analyses of the molecular gas in this sample, we also create morphological classes (i.e. barred, un-barred, and edge-on galaxies) based on optical classifications from Galaxy Zoo and HyperLEDA. By combining our morphological sub-samples with our radial bar-driven flow classifications, we find the following key results:

(i) We find a bar fraction of 0.30 ± 0.08 for the ALMaQUEST sample using our classification procedure outlined in Fig. 2.

(ii) In Fig. 8, we show that 60% ± 15% of the barred sub-sample galaxies are classed as having radial bar-driven flows, compared to 30% ± 10% and 38% ± 13% of the un-barred and edge-on sub-samples, respectively. This suggests that gas flows resembling radial bar-driven flows are more common in galaxies hosting axi-asymmetric features like bars.

(iii) 90% ± 9% of our barred sub-sample galaxies have a multicomponent surface brightness profile as the best-fitting model to their molecular gas distribution (see Fig. 9). This is likely indicative of resonant ring structures driven by bars. We also find a greater proportion of our barred sub-sample galaxies have a multicomponent surface brightness profile compared to the barred sub-sample galaxies hosting radial bar-driven flows. This supports a scenario where gas inflows are shorter lived than the timescale over which galactic bars are stable.

(iv) Comparing the radial and transverse velocity components ($\overline{V}_r$ and $\overline{V}_t$) of the radial bar-driven flows used in our models (defined in Section 3.1), in Fig. 10, we find that our barred sub-sample galaxies have $\overline{V}_r / \overline{V}_t \lesssim 1$, but there are much wider spreads of $\overline{V}_r / \overline{V}_t$ ratios in our other morphological sub-samples. This not only implies a dynamical similarity of the molecular gas kinematics in our barred objects, but also suggests that the gas is spiraling inwards, as opposed to just moving radially, in these objects.

(v) The objects in our 'barred + radial flow' subset appear to have suppressed SFEs compared to those of the 'barred + no radial flow' subset and in the un-barred sub-sample (both globally using GSWLC-X2 and WISE values and in their discs using MaNGA IFS; see Figs 11 and 12). The ability to make this distinction, through molecular gas kinematics, goes some way in explaining the tension between various results in the literature regarding SFE-enhancements/suppression in barred galaxies.

(vi) Galaxies in our 'barred + radial flow' subset have consistently concentrated molecular gas distributions compared to those of the other subsets, which all have a wider spread of concentration parameters (see Fig. 13). Again, we interpret this as an indication that the galaxies in the 'barred + radial flow' subset are undergoing a similar kinematic process, whereby gas is driven inwards.

(vii) In Fig. 14, we show that the objects in the 'barred + radial flow' subset are not depleted of molecular gas relative to the other subsets when comparing their respective central molecular gas mass fractions. These galaxies also has a higher median molecular gas mass surface density in their inner 1 kpc than the 'barred + no radial flow' subset (see Fig. 15), suggesting that radial bar-driven inflows may act to centralize gas in these galaxies. Exhaustion of the central molecular gas reservoirs is, therefore, not the reason for the SFR suppression observed in this subset. We speculate that dynamical effects, such as shear, driven by the radial motions of gas may act to quench the centralized gas reservoirs.

In conclusion, we find that barred galaxies are more likely to host radial molecular gas flows, and that the presence of those flows can also alter their large-scale properties, notably their star-forming efficiencies and the central compaction of their molecular gas reservoirs. Despite the molecular gas being more centrally concentrated in barred galaxies with detected radial bar-driven inflows, they do not power central SFR enhancements (at least not while the flows are on-going). Conversely, we find these galaxies appear to have suppressed SFEs both globally and in their discs. From this, we can begin to infer that gas is being drawn inwards, quenching the discs of these galaxies, and increasing their central molecular gas mass surface densities. However, the dynamics of the flows themselves may act to stabilize the molecular gas against fragmentation and

collapse (e.g. through effects like shear), suppressing the SFEs of the galaxies' molecular gas reservoirs.

To further this work, a larger survey of galaxies with high spatial and spectral resolution CO mapping and with high sensitivity is required, as to date these surveys have been limited in size. The resolutions and sensitivity of the data are critical for meaningful kinematic modelling, which we propose is a vital tool for understanding the baryon cycle and its impact on the evolution of barred galaxies.

DATA AVAILABILITY

All ALMaQUEST data products used in this work are available in the ALMA science archive (https://almascience.eso.org/asax/). MaNGA IFS and stellar mass maps are also publicly available in the SDSS Science Archive Server (SAS; https://dr17.sdss.org/sas/). *GALEX* and *WISE* data can be acquired from their respective online data bases (i.e. https://salims.pages.iu.edu/gswlc/ and http://vizier.cds.unistra.fr/ respectively). The NSA data used in this paper can be accessed via the SDSS DR17 website (https://www.sdss4.org/dr17/manga/manga-data/catalogs/#DRPALLFile).

REFERENCES

Baldwin J. A., Phillips M. M., Terlevich R., 1981, PASP, 93, 5
Bertin G., 2014, Dynamics of Galaxies, 2 edn. Cambridge Univ. Press, Cambridge
Blanton M. R., Roweis S., 2007, AJ, 133, 734
Blanton M. R., Kazin E., Muna D., Weaver B. A., Price-Whelan A., 2011, AJ, 142, 31
Bundy K. et al., 2015, ApJ, 798, 7
Cardelli J. A., Clayton G. C., Mathis J. S., 1989, ApJ, 345, 245
Cavanagh M. K., Bekki K., Groves B. A., Pfeffer J., 2022, MNRAS, 510, 5164
Chabrier G., 2003, PASP, 115, 763
Chiba R., Schönrich R., 2021, MNRAS, 505, 2412
Chown R. et al., 2019, MNRAS, 484, 5192
Coelho P., Gadotti D. A., 2011, ApJ, 743, L13
Combes F., 1991, in Combes F., Casoli F., eds, Vol. 146, Dynamics of Galaxies and Their Molecular Cloud Distributions, p. Springer Dordrecht, 255
Combes F., 2001, in Funes J. G., Corsini E. M., eds, ASP Conf. Ser. Vol. 230, Galaxy Disks and Disk Galaxies. Astron. Soc. Pac., San Francisco, p. 213

Combes F. et al., 2014, A&A, 565, A97
Comerón S. et al., 2014, A&A, 562, A121
Cutri R. M. et al., 2021, VizieR Online Data Catalog, p. II/328
Davis T. A. et al., 2013, MNRAS, 429, 534
Davis T. A. et al., 2014, MNRAS, 444, 3427
Davis T. A., Greene J., Ma C.-P., Pandya V., Blakeslee J. P., McConnell N., Thomas J., 2016, MNRAS, 455, 214
Davis T. A. et al., 2018, MNRAS, 473, 3818
Davis T. A., Zabel N., Dawson J. M., 2020, Astrophysics Source Code Library KinMS: Three-dimensional kinematic modeling of arbitrary gas distributions ascl:2006.003
Davis T. A. et al., 2022, MNRAS, 512, 1522
Díaz-García S. et al., 2021, A&A, 654, A135
Egusa F., Hirota A., Baba J., Muraoka K., 2018, ApJ, 854, 90
Eliche-Moral M. C., González-García A. C., Balcells M., Aguerri J. A. L., Gallego J., Zamorano J., Prieto M., 2011, A&A, 533, A104
Ellison S. L., Nair P., Patton D. R., Scudder J. M., Mendel J. T., Simard L., 2011, MNRAS, 416, 2182
Ellison S. L., Lin L., Thorp M. D., Pan H.-A., Scudder J. M., Sánchez S. F., Bluck A. F. L., Maiolino R., 2021, MNRAS, 501, 4777
Ellison S. L. et al., 2024, MNRAS, 527, 10201
Fang J. J., Faber S. M., Koo D. C., Dekel A., 2013, ApJ, 776, 63
Fraser-McKelvie A. et al., 2020, MNRAS, 495, 4158
French K. D., Yang Y., Zabludoff A., Narayanan D., Shirley Y., Walter F., Smith J.-D., Tremonti C. A., 2015, ApJ, 801, 1
Gadotti D. A., Coelho P., 2015, Highlights Astron., 16, 339
Gadotti D. A., de Souza R. E., 2006, ApJS, 163, 270
Gavazzi G. et al., 2015, A&A, 580, A116
Gensior J., Kruijssen J. M. D., Keller B. W., 2020, MNRAS, 495, 199
Géron T., Smethurst R. J., Lintott C., Kruk S., Masters K. L., Simmons B., Stark D. V., 2021, MNRAS, 507, 4389
Géron T. et al., 2023, MNRAS, 521, 1775
Heitsch F., Slyz A. D., Devriendt J. E. G., Burkert A., 2006, MNRAS, 373, 1379
Hogarth L. M., Saintonge A., Davis T. A., 2023, MNRAS, 518, 13
Janowiecki S., Catinella B., Cortese L., Saintonge A., Brown T., Wang J., 2017, MNRAS, 466, 4795
Jarrett T. H. et al., 2013, AJ, 145, 6
Jogee S., Scoville N., Kenney J. D. P., 2005, ApJ, 630, 837
Kauffmann G. et al., 2003, MNRAS, 341, 54
Kennicutt R. C., Jr, 1998, ARA&A, 36, 189
Kruijssen J. M. D., Longmore S. N., Elmegreen B. G., Murray N., Bally J., Testi L., Kennicutt R. C., 2014, MNRAS, 440, 3370
Krumholz M. R., Kruijssen J. M. D., 2015, MNRAS, 453, 739
Kuno N., Nishiyama K., Nakai N., Sorai K., Vila-Vilaró B., Handa T., 2000, PASJ, 52, 775
Kuno N. et al., 2007, PASJ, 59, 117
Lelli F., Davis T. A., Bureau M., Cappellari M., Liu L., Ruffa I., Smith M. D., Williams T. G., 2022, MNRAS, 516, 4066
Lin L. et al., 2020, ApJ, 903, 145
Lin L. et al., 2022, ApJ, 926, 175
López-Cobá C., Sánchez S. F., Lin L., Anderson J. P., Lin K.-Y., Cruz-González I., Galbany L., Barrera-Ballesteros J. K., 2022, ApJ, 939, 40
Lu S. et al., 2022, ApJ, 927, 215
Maeda F., 2023, IAU Symposium, 373, 207
Maeda F., Ohta K., Fujimoto Y., Habe A., Ushio K., 2020, MNRAS, 495, 3840
Maeda F., Egusa F., Ohta K., Fujimoto Y., Habe A., 2023, ApJ, 943, 7
Makarov D., Prugniel P., Terekhova N., Courtois H., Vauglin I., 2014, A&A, 570, A13
Martig M., Bournaud F., Teyssier R., Dekel A., 2009, ApJ, 707, 250
Martig M. et al., 2013, MNRAS, 432, 1914

Masters K. L. et al., 2011, MNRAS, 411, 2026
Meidt S. E. et al., 2013, ApJ,779, 45
Meidt S. E. et al., 2012, ApJ, 8, 139
Meidt S. E. et al., 2020, ApJ, 892, 73
Nair P. B., Abraham R. G., 2010, VizieR Online Data Catalog, p. J/ApJS/186/427
Olsson E., Aalto S., Thomasson M., Beswick R., 2010, A&A, 513, A11
Pettini M., Pagel B. E. J., 2004, MNRAS, 348, L59
Saintonge A., Catinella B., 2022, ARA&A, 60, 319
Saintonge A., Tacconi L. J., Fabello S., Wang J., Catinella B. et al., 2012, ApJ, 758, 73
Saintonge A., Catinella B., Cortese L., Genzel R., Giovanelli R. et al., 2016, MNRAS, 462, 1749
Sakamoto K., Okumura S. K., Ishizuki S., Scoville N. Z., 1999, ApJ, 525, 691
Salak D., Tomiyasu Y., Nakai N., Kuno N., Miyamoto Y., Kaneko H., 2017, ApJ, 849, 90
Salim S. et al., 2016, ApJS, 227, 2
Salim S., Boquien M., Lee J. C., 2018, ApJ, 859, 11
Sánchez S. F. et al., 2016, RMxAA, 52, 171
Sánchez S. F. et al., 2018, RMxAA, 54, 217
Sánchez S. F. et al., 2022, ApJS, 262, 36
Schinnerer E. et al., 2023, ApJ, 944, L15
Shen J., Sellwood J. A., 2004, ApJ, 604, 614
Shlosman I., Frank J., Begelman M. C., 1989, Nature, 338, 45
Sormani M. C., Barnes A. T., 2019, MNRAS, 484, 1213
Sormani M. C., Binney J., Magorrian J., 2015, MNRAS, 454, 1818
Sormani M. C., Treß R. G., Ridley M., Glover S. C. O., Klessen R. S., Binney J., Magorrian J., Smith R., 2018, MNRAS, 475, 2383
Sormani M. C. et al., 2023, MNRAS, 523, 2918
Spekkens K., Sellwood J. A., 2007, ApJ, 664, 204
Spinoso D., Bonoli S., Dotti M., Mayer L., Madau P., Bellovary J., 2017, MNRAS, 465, 3729
Tacchella S., Dekel A., Carollo C. M., Ceverino D., DeGraf C., Lapiner S., Mandelker N., Primack Joel R., 2016, MNRAS, 457, 2790
Toomre A., 1964, ApJ, 139, 1217
Topal S., Bureau M., Davis T. A., Krips M., Young L. M., Crocker A. F., 2016, MNRAS, 463, 4121
Walmsley M. et al., 2022, MNRAS, 509, 3966
Wang J. et al., 2012, MNRAS, 423, 3486
Watanabe Y., Sorai K., Kuno N., Habe A., 2011, MNRAS, 411, 1409
Willett K. W. et al., 2013, MNRAS, 435, 2835
Woo J., Dekel A., Faber S. M., Koo D. C., 2015, MNRAS, 448, 237
Wright E. L. et al., 2010, AJ, 140, 1868
Yu S.-Y. et al., 2022, A&A, 666, A175
Zolotov A. et al., 2015, MNRAS, 450, 2327
de Vaucouleurs G., de Vaucouleurs A., Corwin H. G. J., Buta R. J., Paturel G., Fouque P., 1991, S&T, 82, 621

SUPPORTING INFORMATION

Supplementary data are available at *MNRAS* online.

suppl_data

Please note: Oxford University Press is not responsible for the content or functionality of any supporting materials supplied by the authors. Any queries (other than missing material) should be directed to the corresponding author for the article.

This paper has been typeset from a TEX/LATEX file prepared by the author.